

UC San Diego

UC San Diego Electronic Theses and Dissertations

Title

Linear acoustic sensitivity kernels and their applications in shallow water environments

Permalink

<https://escholarship.org/uc/item/6zf7m22p>

Author

Sarkar, Bikramjit

Publication Date

2011

Peer reviewed|Thesis/dissertation

UNIVERSITY OF CALIFORNIA, SAN DIEGO

**Linear acoustic sensitivity kernels and their applications in shallow
water environments**

A dissertation submitted in partial satisfaction of the
requirements for the degree
Doctor of Philosophy

in

Oceanography

by

Bikramjit Sarkar

Committee in charge:

William A. Kuperman, Chair
Bruce D. Cornuelle, Co-Chair
William A. Coles
William S. Hodgkiss
Peter F. Worcester

2011

Copyright
Bikramjit Sarkar, 2011
All rights reserved.

The dissertation of Bikramjit Sarkar is approved, and
it is acceptable in quality and form for publication on
microfilm and electronically:

Co-Chair

Chair

University of California, San Diego

2011

TABLE OF CONTENTS

Signature Page	iii
Table of Contents	iv
List of Figures	vi
Acknowledgements	xii
Vita and Publications	xiv
Abstract of the Dissertation	xv
Chapter 1 Introduction	1
References	3
Chapter 2 Information and linearity of time-domain, complex-demodulated, amplitude and phase data in shallow water	5
2.1 Introduction	6
2.2 The Perturbed Green's Function	8
2.2.1 Time domain perturbations	9
2.2.2 Pressure-kernel derivatives for magnitude and phase	10
2.3 Sensitivity Kernels	11
2.3.1 Linearity	15
2.3.2 Information content	18
2.4 Inverting for sound speed changes	22
2.4.1 Numerical example	25
2.5 Discussion and Conclusions	28
2.A Adjoints, kernels, and inverse techniques	30
References	33
Chapter 3 The phase sensitivity kernel and its performance as a linear travel-time estimator	36
3.1 Introduction	37
3.2 The sensitivity kernel equations	38
3.3 Linearity and performance tests	40
3.3.1 Test results presentation format	41
3.3.2 Linearity figures and discussion	45
3.3.3 Phase and travel-time sensitivity differences	50
3.3.4 Statistics from a time-evolving ocean state	56
3.4 Discussion and Conclusions	60
References	61

Chapter 4	Sensitivity kernel for surface scattering in a waveguide	63
4.1	Introduction	63
4.2	The Surface Sensitivity Kernel (SSK)	65
4.3	Experimental measurement of surface sensitivity	69
4.3.1	Tank data vs. synthetic point-to-point SSK	72
4.3.2	Double beamforming treatment	75
4.4	Conclusion	79
	References	80
Chapter 5	Conclusions	82

LIST OF FIGURES

Figure 2.1:	PE model calculations for the pressure field at 1 km from a broadband (3-4 kHz) source at depth 50 m, in a 100 m deep Pekeris waveguide. (a): Depth-Time arrival structure from the numerical results, with a color scale that shows transmission loss in dB. (b): Pressure vs. Time for a receiver at 50 m depth in the arrival structure given above. Amplitude units here are arbitrary with respect to the PE model, where the source pulse had a peak magnitude of 1.	13
Figure 2.2:	Pressure sensitivity kernels (PSK) for arrivals 1, 2 and 3, as marked in Fig. 2.1b, evaluated only in the source-receiver plane. Color scale represents change in received pressure, per unit change in sound speed. Each pixel is the integrated contribution over a unit volume element ($\Delta x = 5$ m, $\Delta z = 0.05$ m), hence no m^{-2} . The units for pressure are arbitrary with respect to the PE model.	14
Figure 2.3:	These 3 graphs plot $\Delta\hat{p}(t)$ (blue) and $\Delta p(t)$ (red) on the same time-base, for increasing values of $\max(\Delta c)$. The time window encompasses the pulse-width of arrival #1 in Fig. 2.1b to show the linear increase in the kernel estimate ($\Delta\hat{p}(t)$) vs the actual. Note the change in scale for the amplitude (vertical) axis, moving from the first (top) panel down.	17
Figure 2.4:	RMS differences between the kernel estimate, $\Delta\hat{p}(t)$, and the direct simulated change, $\Delta p(t)$, for increasing values of $\max(\Delta c)$, where the mean is taken across the whole signal. This provides a quantitative view of the divergence seen in Fig. 2.3, but across the entire time series, and also shows the benefit of working with the envelope of the signal.	18
Figure 2.5:	The evolution of peak arrival #3 (in Fig. 2.1) as the scale of a gaussian perturbation in the center of the environment is increased. The green lines, with circular markers, plot the perturbed PE results while the blue lines, with cross markers, indicate the linear kernel estimated changes. Panel (a) presents the changes in the raw pressure value at arrival #3, and its associated kernel. Panels (b) and (c) show the equivalent results for the demodulated (envelope) magnitude and phase quantities, respectively. Note, in panel (a) the perturbed PE output oscillates around the 0-line as the wave-packet within the peak shifts, but this is obscured by how much the raw pressure kernel overestimates the changes.	19

Figure 2.6:	Sensitivity kernels for envelope/amplitude (a) and phase (b), for arrival 1 as marked in Fig. 2.1b	20
Figure 2.7:	Panels (a) and (b) show the 2D spatial Fourier transforms of the magnitude and phase kernels, respectively, given in Fig. 2.6 for arrival #1. Panels (c) and (d) are the equivalent spectrums for arrival #3 in Fig. 2.1b. The color values describe a logarithmic scale ($20 \log_{10}$) for the magnitude of the FFT output, to compress the dynamic range of the visible features, and do not represent a power-spectral density (PSD).	21
Figure 2.8:	FAF05 profiles for temperature (a), salinity (b) and sound speed (c) showing mean (vertical dashed line) and thermocline (horizontal dashed line). These profiles are the average of several CTD casts, and the resulting sound speed profile has been smoothed prior to use in numerical simulations.	23
Figure 2.9:	(a): Sound speed perturbation map used to generate data. Constructed with 10 vertical internal wave modes and 80 horizontal functions (800 total components). (b): Expected perturbation field when limited to the 20 largest horizontal modes. (c): Inversion result for the perturbation field, using both complex demodulated amplitude and phase data. The estimation process utilized all 10 vertical modes, but limited to the first 20 horizontal functions - 200 total unknowns to determine.	26
Figure 2.10:	Error in inversion estimate vs. assumed SNR ($N_{kx} = 20$) (a), and # of horizontal components (b). Solid lines describe the estimation with data generated via the perturbed PE model; dashed lines are the kernels self-reflected output, i.e. best case. The error value is determined via a 0,0 lag 2D correlation coefficient of the actual and estimated sound speed perturbation maps. The broken black line in both plots, indicates the loss of information expected from the reduced spatial component set alone.	29
Figure 3.1:	Numerical results from a Parabolic Equation (PE) simulation of a 1 km wide, 120 m deep waveguide, using a summer sound-speed profile derived from the FAF05 experiment CTD observations (Fig. 3.2). The top panel shows the arrival structure associated with a source placed 45 m below the surface. The subsequent plots show the individual pressure-time series (complex envelope) from four receiver elements at depths of 15 m, 45 m, 75 m, and 105 m - with significant peaks identified and marked, so that they can be referred to later.	42

Figure 3.2:	FAF05 profiles for temperature (a), salinity (b) and sound speed (c) showing mean (vertical dashed line) and thermocline (horizontal dashed line). These profiles are the average of several CTD casts, and the resulting sound speed profile has been smoothed prior to use in numerical simulations.	43
Figure 3.3:	Sound-speed perturbations used to probe the performance and linearity of the three sensitivity kernel types. (a): Symmetrical Gaussian sound-speed displacement, with spatial scales of 100m in range and 50m in depth, located in the center of the waveguide. (b): Internal-wave induced sound-speed perturbation for the FAF05 summer profile (Fig. 3.2). Vertical modes are derived from buoyancy parameters measured at sea. Horizontal components are sine and cosine functions. The red star marks the source position (at 45 m depth) used in the numerical simulations presented. The color scale indicates the sound-speed shift in m/s.	44
Figure 3.4:	For peak #3 (marked red) in the 15 m time series from Fig. 3.1. This arrival time corresponds to a single ray path, with one bottom-reflection and another surface reflection adjacent to the receiver. Please refer to the end of Sec. 3.3.1 for a detailed description of these plots.	47
Figure 3.5:	For peak #2 (marked green) in the 45 m time series from Fig. 3.1. This arrival time corresponds to a single bottom-reflected symmetric path. Please refer to the end of Sec. 3.3.1 for a detailed description of these plots.	48
Figure 3.6:	For peak #4 (marked teal) in the 75 m time series from Fig. 3.1. This arrival time corresponds to a doubly-reflected single ray path through the environment. Please refer to the end of Sec. 3.3.1 for a detailed description of these plots.	49
Figure 3.7:	For peak #7 (marked black) in the 105 m time series from Fig. 3.1. This arrival time corresponds to the last, and weakest high-angle path. Please refer to the end of Sec. 3.3.1 for a detailed description of these plots.	51
Figure 3.8:	Phase and time sensitivity kernel difference map $(w_c \frac{\partial \tau}{\partial c} - \frac{\partial \theta}{\partial c})$, for peak #2 (marked green) in the 45 m time series from Fig. 3.1. Note the loss of sensitivity along the main beam path that results from the subtraction. The linearity test results for this particular peak are provided in Fig. 3.5.	52

Figure 3.9:	Example data tracks from perturbing the numerical models with phase-time sensitivity difference maps (increased up to ± 2 m/s), such as the one shown in Fig. 3.8. PE observations are plotted with “o” markers, primary kernel estimates as “x” symbols, and secondary estimates with “+” markers. Primary estimates are Phase from Phase kernel, Time from Time kernel; secondary estimates are Phase from Time kernel, and Time from Phase kernel. The results are presented as a table of figures, with column labels indicating the data type plotted, while the rows identify the particular peak (from Fig. 3.1) being tracked. Each peak has been perturbed by its own corresponding difference map. Amplitude units are arbitrary with respect to the numerical model, phase is plotted in radians, and time is shown as the change from the unperturbed value in milliseconds.	54
Figure 3.10:	Envelope for peak #2 (marked green) in the 45 m time series from Fig. 3.1. The solid black curve represents the unperturbed peak pulse shape, marked in time by the broken black vertical line. The solid red curve shows the pulse shape after the environment has been perturbed by the difference map shown in Fig. 3.8, at a magnitude of 2 m/s. The broken red vertical line marks the shift in time of the peak as expected from the TSK estimate.	55
Figure 3.11:	Example data tracks from the time-evolving ocean-state tests (with perturbation magnitude ± 3 m/s) presented as a table of figures, with a layout identical to Fig. 3.9. There are 200 total time steps over 20 independent random ocean states, but just 50 points towards the center of the series are presented here as an example to show the variability. The subplot titles show the Fraction of Variance Explained (FVE), or Coefficient of Determination, as a percentage, for the associated estimate - which is a measure of kernel performance. Amplitude units are arbitrary with respect to the numerical model, phase is plotted in radians, and time is shown as the change from the unperturbed value in milliseconds.	57

Figure 3.12: Summary statistics for the time-evolving ocean-state tests. The histograms show percentage of data for which each estimator can predict most of the observed variability ($FVE > 0.9$), plotted against increasing perturbation magnitude. In the phase and time diagrams, the blue bars represent the time kernel performance; the red bars are for the phase kernel metrics. Each row shows the same statistics recalculated with different data filtering choices. Excluding multipath keeps only those peaks associated with a single eigenray. Excluding weak peaks retains only the 1st five significant arrivals, throwing out later high-angle peaks. The last column of plots, labeled “PE Time-Phase” show how well observed variations in (peak) travel-time can be explained by observed phase changes. 59

Figure 4.1: Schematic diagram showing the dimensions of the laboratory tank experiment.
 (a) - The source/receiver coplanar arrays consist of 64 ultrasonic transducer-elements, each of size $0.75 \text{ mm} \times 12 \text{ mm}$ (*vertical* \times *horizontal*). The source-receiver arrays span the whole water column.
 (b) - A 5 mm lead sphere serves as a probe to impact the air-water interface [black arrow in (a)]. The penetration of the sphere inside the waveguide is on the order of one millimeter. Acquisitions between the source-receiver arrays are performed in the time domain for probe positions varying sequentially from the source-array to the receiver-array in 1 mm increments. . . . 71

Figure 4.2: (a) - Envelope of the time-domain impulse response across the receiver-array as measured in the tank for a pulse transmission from element #32 on the source-array. Color scale represents normalized pressure.
 (b) - Normalized pressure-time series as measured on receiver element #32 (broken line), and equivalent double beamformer output from focusing two source-receiver subarrays on the eigenray path (with grazing-angle incidence $\sim 5^\circ$) identified as number 1 in Fig. 4.4 (solid line).
 (c) - Magnified plot of the peak-time around the single wavepacket produced in the double beamformer output (solid line), with the equivalent view of the perturbed data set (broken line) resulting from the presence of the probe at the surface at range 300 mm. Note the small amplitude and travel-time change (on the order of a few %) associated with this low grazing-angle incident eigenray. 73

- Figure 4.3: (a) - Experimental surface sensitivity (intensity), produced by the difference between 'up' and 'down' field measurements when the probe is raised and lowered, plotted as a function of probe position in range r' .
(b) - Theoretical surface sensitivity (intensity) calculated by Eq. 4.7 and convolved with the surface perturbation shape, $\Delta h(r')$, to better approximate the experimentally observed sensitivity. Color scales represent the induced change in measured pressure in arbitrary linear units, normalized to the maximum of each plot. 74
- Figure 4.4: Eigenray paths associated with the geometry between source #32 and receiver #32 show which paths interact with the surface, and at what locations. Path #s 1 and 2 correspond to one bounce and two bounces at the water-air interface, respectively. Path #3 is the symmetric equivalent of #2, with two surface bounces as well, but with opposite launch-arrival angles. Though Paths #s 2 and 3 arrive at the same time, their individual contributions may be separated through double beamforming. 75
- Figure 4.5: Double-beamformed results for both experimental and theoretical sensitivity kernels
Panels (a) & (b) show the amplitude and time kernels, respectively, for a steering angle of $+5.05^\circ$ on both arrays. This represents focus on the peak at time $410 \mu\text{s}$ in Fig 4.3, corresponding to the eigenray path number 1 in Fig. 4.4.
Panels (c) & (d) present the equivalent results for the peaks along time $438 \mu\text{s}$ in Fig 4.3, corresponding to the eigenray path number 2 in Fig. 4.4. The steering angles in this case are $+18.07^\circ$ on the source array and -18.07° on the receive array. . . 78

ACKNOWLEDGEMENTS

I wish to thank my advisors, Bill Kuperman and Bruce Cornuelle, for their constant encouragement, support, and infinite patience. Despite their demanding positions and busy schedules, they have always found the time for me, and listening to them chat during our meetings reminds me of all the history in math and physics that has come before everything I work on today.

The other members of my thesis committee have also been very kind to me over the years, and for that I am very grateful: Bill Coles, for taking the time away from his own work and his own department to provide the outside perspective on my research; Bill Hodgkiss and his wonderful classes are responsible for much of the technical knowledge and skills that I’ve accrued and applied in my thesis; and Peter Worcester has always been very welcoming, allowing me attend meetings with his own research group, and willing to hear about some of the quirkier results I may have had to show.

I would also like to thank the many other people here at Scripps who have influenced both my work and my life: from the wonderful folk at the SIO graduate office, who have helped me dot the ‘i’s and cross the ‘t’s as a student; to everyone at the Marine Physical Lab (MPL), who make sure *everything* in our day-to-day lives goes swimmingly—Evelyn Doudera, especially, has been a great source of support, always reminding me to take care of the little things, and to also take a cookie. Finally, my time here would not be complete without the constant company of my fellow students and the many friends I’ve made along the way.

This dissertation is a collection of papers that have been accepted, submitted, or are in preparation for publication.

Chapter 2 is, in full, a reprint of material published in *The Journal of the Acoustical Society of America*: Jit Sarkar, Bruce D. Cornuelle, and William A. Kuperman, “Information and linearity of time-domain, complex-demodulated, amplitude and phase data in shallow water”. The dissertation author was the primary investigator and author of this paper.

Chapter 3 is a manuscript in preparation for submission to *The Journal of the Acoustical Society of America*: Jit Sarkar, Bruce D. Cornuelle, and William A.

Kuperman, “The phase sensitivity kernel and its performance as a linear travel-time estimator”. The dissertation author was the primary investigator and author of this paper.

Chapter 4 is, in full, a reprint of material accepted for publication in *The Journal of the Acoustical Society of America*: Jit Sarkar, Christian Marandet, Philippe Roux, Shane Walker, Bruce D. Cornuelle, and William A. Kuperman, “Sensitivity kernel for surface scattering in a waveguide”. The dissertation author was the primary investigator and author of this paper.

VITA

2003	B.S., Computer Engineering and Computer Science University of Virginia
2010	M.S., Oceanography - Applied Ocean Sciences Scripps Institution of Oceanography, University of California, San Diego
2011	Ph.D., Oceanography - Applied Ocean Sciences Scripps Institution of Oceanography, University of California, San Diego
2003-2010	Graduate Student Researcher Marine Physical Laboratory, University of California, San Diego

PUBLICATIONS

Journals

1. Jit Sarkar, Christian Marandet, Philippe Roux, Shane Walker, Bruce D. Cornuelle, and William A. Kuperman, "Sensitivity kernel for surface scattering in a waveguide", *J. Acoust. Soc. Am.*, submitted.
2. Jit Sarkar, Bruce D. Cornuelle, and William A. Kuperman, "Information and linearity of time- domain, complex-demodulated, amplitude and phase data in shallow water", *J. Acoust. Soc. Am.*, accepted.

Conferences

1. Jit Sarkar, Bruce Cornuelle, Philippe Roux, and W. A. Kuperman, "Fréchet-derivative calculations of the environmental sensitivity of the arrival structure in shallow water", *J. Acoust. Soc. Am.* Volume 116, Issue 4, pp. 2558-2558 (2004)
2. Jit Sarkar, Bruce Cornuelle, Philippe Roux, W. S. Hodgkiss, W. A. Kuperman, and Mark Stevenson, "Converting sound-speed uncertainty to an effective correlated noise term in array processing", *J. Acoust. Soc. Am.* Volume 117, Issue 4, pp. 2462-2462 (2005)
3. Jit Sarkar, Bruce Cornuelle, W. A. Kuperman, and Philippe Roux, "Estimating sound-speed perturbations with full-wave environmental sensitivity kernels", *J. Acoust. Soc. Am.* Volume 119, Issue 5, pp. 3246-3246 (2006)
4. Jit Sarkar, Shane Walker, Bruce Cornuelle, William A. Kuperman, Philippe Roux, and Christian Marandet, "Inverting for surface displacement fields using directly measured point-to-point sensitivity kernels", *J. Acoust. Soc. Am.* Volume 127, Issue 3, pp. 1939-1939 (2010)

ABSTRACT OF THE DISSERTATION

**Linear acoustic sensitivity kernels and their applications in shallow
water environments**

by

Bikramjit Sarkar

Doctor of Philosophy in Oceanography

University of California, San Diego, 2011

William A. Kuperman, Chair

Bruce D. Cornuelle, Co-Chair

Time of arrival information from acoustic transmissions is the primary means through which ocean sound-speed structure is estimated. While initially limited to large scale coarse observations using ray theory to model the propagation of sound through the environment, ocean acoustic tomography evolved to incorporate a normal-mode representation of observed peak-arrivals. This wave-theoretic approach was enhanced, using the first Born approximation to perturbations in the wave equation, producing the travel-time sensitivity kernel (TSK): a linear relationship between sound-speed variations and observed changes in arrival times.

This dissertation extends sensitivity kernel analysis to both the amplitude and phase of complex- demodulated broadband acoustic transmissions, producing both a qualitative and quantitative picture of how ocean sound-speed variability affects acoustic observations, and complementing prior work on travel-time sensitivity. The linearity and information content of these kernels is explored in simulation for a 3–4 kHz broadband pulse transmission through a 1 km shallow-water Pekeris waveguide, and in simulated inversions with a more realistic summer-type sound-speed profile, the results from which demonstrate the additional information amplitude contains over phase data alone.

Differences in phase measurements were assumed to be directly relatable to travel-time changes, and thus the phase sensitivity kernel was expected to represent the same details as the travel-time sensitivity kernel. However, even a cursory visual inspection of the two kernel types shows that they have different spatial structures and hence different sensitivities to changes in the environment. A numerical survey was conducted comparing the performance of these sensitivity kernels (along with amplitude) to observations from perturbed simulations - including a synthetic time-evolving ocean - and the results suggest that phase and peak travel-time do indeed diverge in the presence of more complicated ocean sound-speed structure, with phase being the more linear observable. Additionally, the phase-derived sensitivity kernel is shown to be a better estimator of travel-time than the TSK, for which a possible explanation is suggested.

The Born approximation has also been used to derive the acoustic sensitivity to perturbations at the boundary of an environment, in contrast to the volume perturbations discussed before. A sensitivity kernel for surface scattering is presented here, along with a numerical and experimental investigation of the acoustic response to surface displacements in an ultrasonic scale waveguide. The results are presented in both point-to-point and beam-to-beam formats, and suggest the potential use of sensitivity analysis in inverting for sea-surface structure.

Chapter 1

Introduction

The use of acoustic signals to probe the interior structure of the oceans was first proposed by Munk and Wunsch[1], laying the foundations of the field of ocean acoustic tomography. Their scheme used the differences in travel-time measurements from repeated acoustic transmissions to invert for the sound-speed changes in the intervening ocean volume by relating the observations to geometric ray paths. While adequate for inferring coarse large-scale features, ray theory is a high-frequency asymptotic approximation that may not be applicable to low-frequency limited bandwidth acoustic signals. To this end, the ray view of acoustic propagation was supplemented with normal-mode representations[2, 3], which helped identify observed arrivals not easily associated with an expected ray path. Eventually, a wave-theoretic approach to acoustic tomography was explored that did not require observed peaks to be identified as either rays or modes[4, 5], leading to the development of the travel-time sensitivity kernel (TSK)[6]: a linearized representation of the effect sound-speed fluctuations have on observed peak arrival times, given by the first Born approximation to a perturbation in the full wave equation.

“Travel time” has been the key phrase repeated while discussing the history of ocean acoustic tomography. The amplitude of an observed peak is rarely mentioned in long-range tomographic applications, because its sensitivity to sound speed is considered too non-linear to be of use. However, data collected during a short-range acoustic experiment in the Mediterranean Sea, the Focused Acoustic

Fields experiment of 2005 (FAF05), showed amplitude observations stable enough to potentially be useful for tomographic inversions. This provides the motivation for the work presented in Chapter 2 of this dissertation, where the sensitivity analysis previously performed for travel time is extended to the amplitude and phase of a broadband acoustic signal. The sensitivity kernels are derived relative to the complex demodulated representation of the signal, from which the amplitude and phase quantities are obtained, and shown to be more linear than working with raw pressure directly. The information content of these kernels is explored in simulation for a 3–4 kHz broadband pulse transmission through a 1 km shallow-water Pekeris waveguide, employing a split-step Padé parabolic equation (PE)[7] numerical model for the acoustic propagation. The kernels are also used in simulated inversions with a more realistic summer-type sound-speed profile. The results of these investigations indicate that amplitude data contains information about the environment that is supplementary to what phase data can provide alone.

Phase itself is presumed to be a linear function of travel time, determined through the inclusion of a frequency factor, ω . Yet the equation for phase sensitivity, derived in Chapter 2, is not directly relatable to the equation for travel-time sensitivity, as presented by Skarsoulis and Cornuelle[6]. Chapter 3 explores the differences between these two kernels by investigating their performance as linear estimators (along with the amplitude sensitivity kernel), comparing the results to the output of perturbed numerical simulations. These tests progress from a uniform sound-speed increase across the whole environment, to an artificial range-dependent displacement, and finally a synthetically generated time-evolving ocean sound-speed state, based on experimentally observed buoyancy parameters (FAF05). The results show that, despite the differences in formulation and spatial appearance, the phase and travel-time sensitivity kernels provide nearly identical estimates of the change in observed acoustic response, but only with respect to large-scale perturbations. As the complexity of the sound-speed structure increases, the two measures begin to diverge – a trend seen in both the kernel estimates and the synthetic observations from the perturbed simulations. Further investigation of their differences in structure indicate that much of the extra sen-

sitivity apparent in the TSK is not representative of finite-perturbation-amplitude travel-time variability, and that the phase-derived sensitivity kernel is a better measure of travel-time changes over a range of realistic perturbation sizes.

The acoustic sensitivities discussed thus far have been focused on sound-speed changes – volumetric perturbations within the environment. The Born approximation can also be applied to changes in the boundaries of an environment, and Chapter 4 derives one such linearized sensitivity kernel for the relationship between point displacements along the surface of a waveguide and the acoustics propagating within. This surface scattering kernel is investigated for an ultrasonic-scale waveguide in a laboratory tank experiment where the the surface is directly perturbed on a point-by-point basis and the effect on acoustic propagation observed. The results are compared with theoretical calculations for the surface sensitivity, determined with a PE numerical model, showing substantial agreement. This suggests that the surface sensitivity kernel may be used to efficiently incorporate surface effects in forward numerical models of acoustic propagation and could also be used in inverting for sea-surface structure.

References

- [1] Walter H Munk and Carl Wunsch. Ocean acoustic tomography: a scheme for large scale monitoring. *Deep-Sea Res.*, 26(1):23–21, 1979.
- [2] Walter H Munk and Carl Wunsch. Ocean Acoustic Tomography: Rays and Modes. *Rev. Geophys. Space Phys.*, 21(4):777–793, 1983.
- [3] E C Shang. Ocean acoustic tomography based on adiabatic mode theory. *J. Acoust. Soc. Am.*, 85(4):1531–1537, 1989.
- [4] Gerassimos A Athanassoulis and Emmanuel K Skarsoulis. Arrival-time perturbations of broadband tomographic signals due to sound-speed disturbances. A wave-theoretic approach. *J. Acoust. Soc. Am.*, 97(6):3575–3588, 1995.
- [5] Emmanuel K Skarsoulis, Gerassimos A Athanassoulis, and Uwe Send. Ocean acoustic tomography based on peak arrivals. *J. Acoust. Soc. Am.*, 100(2):797–813, 1996.
- [6] Emmanuel K Skarsoulis and Bruce D Cornuelle. Travel-time sensitivity kernels in ocean acoustic tomography. *J. Acoust. Soc. Am.*, 116(1):227–238, 2004.

- [7] Michael D Collins. A split-step Padé solution for the parabolic equation method. *J. Acoust. Soc. Am.*, 93(4):1736–1742, 1993.

Chapter 2

Information and linearity of time-domain, complex-demodulated, amplitude and phase data in shallow water

Abstract

Wave-theoretic ocean acoustic propagation modeling is used to derive the sensitivity of pressure, and complex demodulated amplitude and phase, at a receiver to the sound speed of the medium using the Born-Fréchet derivative. Although the procedure can be applied for pressure as a function of frequency instead of time, the time domain has advantages in practical problems, since linearity and signal-to-noise are more easily assigned in the time domain. The linearity and information content of these sensitivity kernels is explored for an example of a 3-4 kHz broadband pulse transmission in a 1 km shallow water Pekeris waveguide. Full-wave observations (pressure as a function of time) are seen to be too nonlinear for use in most practical cases, while envelope and phase data have a wider range of validity and provide complementary information. These results are used in simulated inversions with a more realistic sound speed profile, comparing the

performance of amplitude and phase observations.

2.1 Introduction

Both pulsed and pure tone acoustic transmissions have been used in a variety of ways to estimate ocean and bottom structure. An example of pulsed signals is ocean acoustic tomography, suggested by Munk and Wunsch[1, 2] to monitor the time-evolving large-scale ocean structure using travel times measured by transmitting pulsed sound in the 50-300 Hz range to distant receivers. In spite of the low frequencies used in experiments, the high-frequency ray approximation was employed in analysis so that arrival times were assumed to sample the ocean along idealized ray paths through the water column. Given enough diverse paths traversing the medium, the ocean sound speed structure can then be reconstructed.

As an alternative to ray-theoretic modeling of travel times, wave-theoretic approaches have been employed, such as the modal-arrival[3, 4] and the peak arrival approach[5, 6]. This led to the development of the Travel time Sensitivity Kernel (TSK)[7], a first-order linearization of the influence sound speed variations have on acoustic propagation via the wave equation. TSK analysis, and previous seismological literature[8, 9], moved away from the high-frequency assumption to provide a wave-theoretic relation between a time of arrival and the parts of the medium that affect it. These kernels have also been extended to include array processing techniques to produce beamformed analogs of the TSK[10]. However, the drawback to sensitivity kernel analysis is its linearity, which limits the size of the perturbations for which the kernels are valid.

Acousticians have also transmitted pure tones and used the amplitude and phase of the received signal for geoacoustic inversion[11, 12]. In this procedure, forward models are combined with linear and nonlinear optimization methods[13, 14, 15] to search for the global extremum representing the estimated geoacoustic properties in a multidimensional parameter landscape. In contrast to sensitivity kernel analysis, this global optimization procedure does not generally provide a physical picture of the dependence of the observations on perturbations to the medium.

More closely related to the sensitivity analysis is the adjoint method[16, 17] which gives the gradients for an iterative linear descent algorithm to fit the observations by perturbing the medium. The gradient for a single observation is equivalent to the sensitivity kernel, but to date, authors have generally focused on estimating the medium, and considered all observations together, limiting physical interpretation of the results though still requiring linearity to be valid. The adjoint method has been previously explored in a ‘broadband’ sense using multiple independent frequencies[18, 19], and has also been theoretically investigated in the time-domain[20]. Amplitude data in broadband tomographic work has been avoided this far, because its sensitivity to sound-speed becomes strongly nonlinear over long ranges; however, recent short-range acoustic experiments[21] have exhibited recorded amplitudes stable enough over multiple measurements for use in tomographic inversions. In the previous work discussed above, there has been no discussion of the structure of the amplitude and phase sensitivity kernels or their information content, which is explored here.

The present work applies wave-theoretic modeling to obtain the two-dimensional (2D) sensitivity kernel to sound speed for pressure, and pulse envelope amplitude and phase, as a function of time for finite-frequency transmissions. We use the Born-Fréchet kernel of the linear (first-order) integral representation of pressure variations in terms of the spatial distribution of sound speed variation[8]. Such kernels have already been applied to investigate the performance of time-reversal acoustics[22], but are presented here with an eye towards tomographic inversions; investigating the range of linearity, as well as the spatial resolution provided by the kernels. In this paper we apply the sensitivity kernel analysis to the full acoustic wave field to show that pressure amplitude data contain information that *supplements* the standard time of arrival tomographic procedures.

Travel times have been used as the observable in relatively long-range propagation, where only the stationary phase arrivals are linear enough to be used for inversion. In this paper, we show that the amplitude of the pressure field contains useful information as well, at least for small perturbation sizes. Care has been taken to explore the range of linearity, and some types of arrivals are found

to have larger linearity ranges than others. Even though the observed range of linearity for these sensitivity kernels is limited in some examples, it still provides a framework with which to investigate the structure of influence the environment has on acoustic propagation.

We begin Sec. 2.2 by reviewing the Green’s function for ocean acoustic propagation and its perturbations in the Born approximation, along with how this translates to sensitivity kernels of pressure in the time-domain, as well as corresponding magnitude and phase kernels for the demodulated signals. Further, the Appendix relates the sensitivity kernel analysis to the adjoint method. Section 2.3 describes the simulations performed to calculate these kernels and discusses some of the example sensitivity maps shown. Section 2.3.1 investigates the range of linearity for these kernels through the use of perturbed forward model runs to test them against and in Sec. 2.3.2 we explore the additional information provided by full-wave data over travel-time measurements alone. In Sec. 2.4 the problem of inverting pressure records is addressed, with a discussion of the spatial resolution afforded by the kernels. This is followed by some sample inversions performed on simulated data in Sec. 2.4.1. Finally, Sec. 2.5 contains a discussion of results and main conclusions from this work.

2.2 The Perturbed Green’s Function

The results of introducing a perturbation into the Helmholtz equation have already been described in earlier TSK work[7], but are summarized here for completeness.

In the following inhomogeneous Helmholtz equation, the Green’s function $G(\mathbf{r}|\mathbf{r}_s)$ represents the acoustic pressure field response at a position \mathbf{r} , due to a point source located at \mathbf{r}_s :

$$\left[\nabla^2 + \frac{\omega^2}{c^2(\mathbf{r})} \right] G(\mathbf{r}|\mathbf{r}_s) = -\delta(\mathbf{r} - \mathbf{r}_s). \quad (2.1)$$

Here, ω is the circular frequency of the source, $c(\mathbf{r})$ describes the sound-speed distribution, and δ is the Dirac delta-function. The necessary boundary conditions

require that G is identically 0 at the surface, while pressure and normal-velocity are continuous across the interfaces. The radiation condition demands that the field decay with range away from the source, describing an outgoing wave[23].

Perturbing the sound-speed distribution in Eq. (2.1), by an amount, Δc , induces a perturbation in the Green's function, ΔG , that must satisfy the same boundary conditions as the original unperturbed Green's function:

$$\left[\nabla^2 + \frac{\omega^2}{[c(\mathbf{r}) + \Delta c(\mathbf{r})]^2} \right] [G(\mathbf{r}|\mathbf{r}_s) + \Delta G(\mathbf{r}|\mathbf{r}_s)] = -\delta(\mathbf{r} - \mathbf{r}_s). \quad (2.2)$$

Equation (2.2) can be rearranged into a form that resembles the induced pressure-field due to an arbitrary source distribution, interpreted as a ‘new’ set of sources produced at each point, \mathbf{r} , by scattering from the original propagating wave through the perturbed environment. This integral expression is then linearized (retaining only first-order terms) to obtain the Born approximation[24] for the perturbation of the Green's function:

$$\Delta G(\mathbf{r}_r|\mathbf{r}_s) = -2\omega^2 \int_V G(\mathbf{r}'|\mathbf{r}_s) G(\mathbf{r}_r|\mathbf{r}') \frac{\Delta c(\mathbf{r}')}{c^3(\mathbf{r}')} dV(\mathbf{r}'), \quad (2.3)$$

where the volume integral for V is conducted over all positions in the medium, \mathbf{r}' , and for a given receiver position, \mathbf{r}_r . The steps leading from Eq. (2.2) to Eq. (2.3) have been omitted here, as they are described in detail by Skarsoulis *et al.*[7]

The sensitivity (Fréchet derivative[20]) of the Green's function at this frequency to a change in sound-speed at an individual point, \mathbf{r}' , is then:

$$\frac{\partial G(\mathbf{r}_r|\mathbf{r}_s)}{\partial c(\mathbf{r}')} = -2\omega^2 G(\mathbf{r}'|\mathbf{r}_s) G(\mathbf{r}_r|\mathbf{r}') \frac{1}{c^3(\mathbf{r}')}, \quad (2.4)$$

which is comparable to the adjoint of the PE model[16] for the selected frequency (ω) and source-receiver pair (see Appendix). The sensitivity for all points in the region is referred to as the “sensitivity kernel”, since the integral of the kernel multiplied by a sound-speed perturbation is the change in the green's function.

2.2.1 Time domain perturbations

Given the frequency-domain Green's function for propagation to a distant receiver, \mathbf{r}_r , and a source-signal spectrum, $P_s(\omega)$, the acoustic field recorded at the

receiver can be expressed through the inverse Fourier transform,

$$p_r(t) = \frac{1}{2\pi} \int_{-\infty}^{\infty} G(\mathbf{r}_r|\mathbf{r}_s; \omega; c) P_s(\omega) e^{i\omega t} d\omega, \quad (2.5)$$

where we have explicitly included the frequency dependance of G .

Introducing a sound-speed perturbation, Δc , at a point, \mathbf{r}' , will cause a change, ΔG , in the Green's function (given by Eq. (2.3)), and in turn induce a variation, Δp_r , in the acoustic pressure at the receiver in the time domain:

$$\Delta p_r(t) = \frac{1}{2\pi} \int_{-\infty}^{\infty} \Delta G(\mathbf{r}_r|\mathbf{r}_s; \omega; c; \Delta c) P_s(\omega) e^{i\omega t} d\omega. \quad (2.6)$$

Dividing Eq. (2.6) by the perturbation, Δc , yields an integrand that can be substituted with the expression for $\frac{\partial G}{\partial c}$ given in Eq. (2.4), producing an equation for the sensitivity of pressure (in time) to changes in the sound-speed field:

$$\frac{\partial p_r(t)}{\partial c(\mathbf{r}')} = \frac{1}{2\pi} \int_{-\infty}^{\infty} \left(-2\omega^2 G(\mathbf{r}'|\mathbf{r}_s) G(\mathbf{r}_r|\mathbf{r}') \frac{P_s(\omega)}{c^3(\mathbf{r}')} \right) e^{i\omega t} d\omega. \quad (2.7)$$

The formula in Eq. (2.7) constitutes the primary kernel calculated in the work presented below - which we refer to as the Pressure Sensitivity Kernel (or PSK) - and also appears implicitly as an ingredient of the TSK analysis performed by Skarsoulis and Cornuelle[7], but is never explored directly in that work.

2.2.2 Pressure-kernel derivatives for magnitude and phase

The recorded broadband pressure-signal, $p(t)$, can be demodulated with the central/carrier frequency, ω_c , yielding the complex base-banded signal (appropriately filtered):

$$P(t) = p(t) e^{-i\omega_c t}.$$

The sensitivity kernel for pressure, $\frac{\partial p}{\partial c}$, may be similarly demodulated:

$$\frac{\partial P}{\partial c} = \frac{\partial p}{\partial c} e^{-i\omega_c t},$$

where the upper-case P is used to represent the complex demodulated quantities. The envelope of the signal is then obtained from the magnitude of P by

$$|P| = \sqrt{P_r^2 + P_i^2}.$$

Here, P_r and P_i represent the real and imaginary components of P , respectively. To determine the sensitivity of the envelope to sound-speed perturbations, the derivative is taken with respect to c :

$$\frac{\partial |P|}{\partial c} = \frac{1}{2} (P_r^2 + P_i^2)^{-1/2} (2P_r \frac{\partial P_r}{\partial c} + 2P_i \frac{\partial P_i}{\partial c})$$

yielding a formula for magnitude/envelope sensitivity that is a function of the base unperturbed complex pressure, and the associated kernels:

$$\frac{\partial |P(t)|}{\partial c(\mathbf{r}')} = \frac{P_r(t) \left(\frac{\partial P(t)}{\partial c(\mathbf{r}')} \right)_r + P_i(t) \left(\frac{\partial P(t)}{\partial c(\mathbf{r}')} \right)_i}{|P(t)|}. \quad (2.8)$$

Similarly, the phase of the complex broadband pressure-signal is given by

$$\theta = \tan^{-1} \left(\frac{P_i}{P_r} \right),$$

where P_r and P_i are as defined above, and θ is the phase in radians. Differentiating this expression with respect to c , as before,

$$\frac{\partial \theta}{\partial c} = \frac{P_r \frac{\partial P_i}{\partial c} - P_i \frac{\partial P_r}{\partial c}}{P_r^2 + P_i^2},$$

then produces the sensitivity kernel for phase with respect to sound-speed perturbations:

$$\frac{\partial \theta(t)}{\partial c(\mathbf{r}')} = \frac{P_r(t) \left(\frac{\partial P(t)}{\partial c(\mathbf{r}')} \right)_i - P_i(t) \left(\frac{\partial P(t)}{\partial c(\mathbf{r}')} \right)_r}{|P(t)|^2}. \quad (2.9)$$

This is not identical to the expression for the TSK[7], even though the two observables can be closely related

2.3 Sensitivity Kernels

To investigate the information content in a realistic environment, pressure kernels were calculated for a range-independent environment using a Padé parabolic equation (PE) numerical model[25] for the acoustic propagation. A normal-mode based model could have been employed instead, but the choice of a PE solution allows for easy treatment of range-dependent environments.

The simulated environment is 100 m deep, with a flat bottom, and 1km wide. The sound speed profile (SSP) used is 1500 m/s in the water column and 1600 m/s in the bottom - i.e. a Pekeris waveguide. The simulated transmission signal is a broadband linear frequency modulated (LFM) chirp, 3-4 kHz. The depth, range, bottom sound speed, but not the SSP, were chosen to be similar to those encountered at sea during the Focused Acoustic Fields (FAF) experiments conducted in the Mediterranean between 2004 and 2006 in collaboration with the NATO Undersea Research Center (NURC), in anticipation of working with those data sets. The grid density used for the numerical model was set at $\Delta x = 5$ m and $\Delta z = 0.05$ m, but the results only retained every 0.5 m in depth. Smaller steps in range were tested, but did not augment the kernels substantially.

The PE model is used to determine the Green's functions at each frequency required in Eq. (2.5) for calculation of point sensitivities (at \mathbf{r}') in the environment. These frequency kernels are combined through Fourier synthesis to provide the broadband, time-domain pressure sensitivity kernels (PSKs) as per Eq. (2.7). An assumption made in this work to simplify calculations is one of reciprocity: that $G(\mathbf{r}|\mathbf{r}') = G(\mathbf{r}'|\mathbf{r})$. With this in mind, only two forward model runs are required to calculate the kernel: $G(\mathbf{r}'|\mathbf{r}_s)$ - representing propagation of energy away from the source, and $G(\mathbf{r}'|\mathbf{r}_r)$ - propagation away from the receiver. Without this assumption separate model runs would have to be calculated for propagation to the receiver from every point within the intervening medium.

Figure 2.1a shows the arrival structure produced from modeling a broadband source at a depth of 50 m within the above described environment. The horizontal line through the plot represents the depth of a receiver (at 50 m) for which sensitivity kernels will be shown. Figure 2.1b shows the pressure-time record for this receiver, along with markings to label the peak arrivals. Though kernels can be calculated for any point within the given time-series, they are only of use for inversion where there is significant received energy.

Figure 2.2a shows a PSK for the peak of arrival #1 in the pressure-time series for this receiver. The kernel map describes what regions in the medium can influence the value of the pressure received at the peak arrival time. In the color

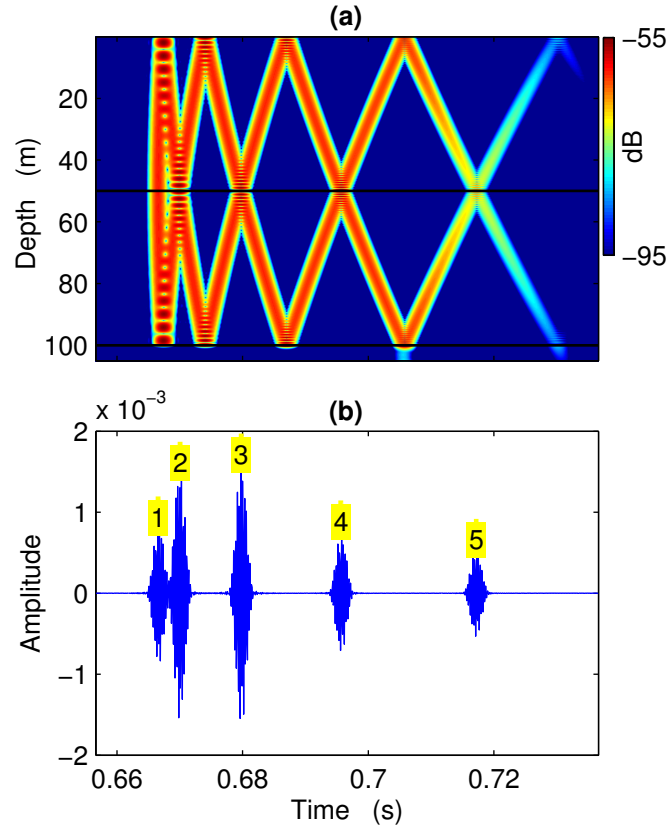


Figure 2.1: PE model calculations for the pressure field at 1 km from a broadband (3-4 kHz) source at depth 50 m, in a 100 m deep Pekeris waveguide.

(a): Depth-Time arrival structure from the numerical results, with a color scale that shows transmission loss in dB.

(b): Pressure vs. Time for a receiver at 50 m depth in the arrival structure given above. Amplitude units here are arbitrary with respect to the PE model, where the source pulse had a peak magnitude of 1.

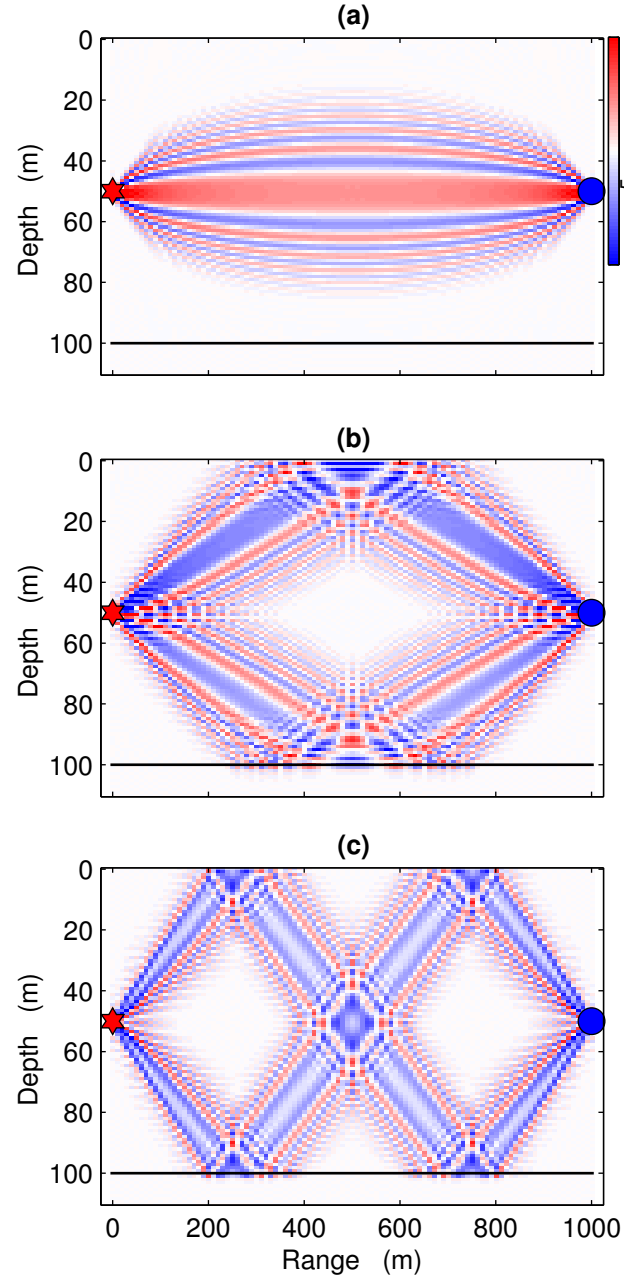


Figure 2.2: Pressure sensitivity kernels (PSK) for arrivals 1, 2 and 3, as marked in Fig. 2.1b, evaluated only in the source-receiver plane. Color scale represents change in received pressure, per unit change in sound speed. Each pixel is the integrated contribution over a unit volume element ($\Delta x = 5$ m, $\Delta z = 0.05$ m), hence no m^{-2} . The units for pressure are arbitrary with respect to the PE model.

scale, red indicates that an increase in sound speed at that point will increase the received pressure, whereas blue indicates that an increase in sound speed will decrease the pressure. Due to the high-frequency and broadband nature of the signal simulated, the picture presented appears somewhat ray-like. This impression continues through the rest of the time-series as well: figures 2.2b and 2.2c present the kernel maps for arrivals 2 and 3 respectively, and the paths of the surface-reflected and bottom-reflected rays can be discerned. Areas of the pressure-time series with no received signal still have associated kernel maps with some structure, but they cannot be intuitively described as rays/modes as in the other cases presented. However it does indicate that given changes in the environment at the significant areas within the kernel map, the observed energy at this point in time can be expected to increase from zero.

2.3.1 Linearity

To investigate the range of linearity of these kernels, a sample sound speed perturbation is introduced to cause a change in the received pressure field. An estimate of this change, $\Delta\hat{p}$, is calculated using the PSK by

$$\Delta\hat{p}(t) = \int_V \frac{\partial p(t)}{\partial c(\mathbf{r}')} \Delta c(\mathbf{r}') dV. \quad (2.10)$$

When the kernel and perturbation quantities are expressed as vectors numerically, this operation becomes an inner (dot) product of the two. To calculate the actual change in received pressure, a second PE model run is performed through a modified environment, with the perturbation applied to the background SSP. The change in received pressure is then

$$\Delta p(t) = p(t) - p_0(t),$$

where p is the perturbed PE solution, and p_0 is the base, unperturbed result.

The perturbation used in these tests is a Gaussian function of both range (x) and depth(z) with a scale of 50 m in both dimensions, and positioned in the center of the domain ($x = 500$ m $z = 50$ m). The linear sensitivity as a function of position of this perturbation has also been studied, and found to be maximal

at the center. The peak magnitude of the sound-speed perturbation is scaled from 1 m/s to 20 m/s, and for each case the difference between $\Delta\hat{p}$ and Δp is observed.

The plots in Fig. 2.3 are magnified around the region of arrival #1 so that differences within the wave-packet are visible. The kernel predicts a linear increase in amplitude with increasing magnitude of the sound-speed perturbation, shown by the increasing scale of the blue curve in Fig. 2.3, but this is not how the actual wavelet behaves for large deviations, as evidenced by the red curve. A root mean square (RMS) error between the estimated pressure change ($\Delta\hat{p}$) and the actual difference (Δp) has been calculated over the entire time series, the results of which are summarized in Fig. 2.4. The values plotted are given by

$$\frac{\sqrt{\langle(\Delta\hat{p}(t) - \Delta p(t))^2\rangle}}{\sqrt{\langle(\Delta p(t))^2\rangle}}$$

where the mean, denoted by $\langle \rangle$, is taken across all time and the resulting fraction expressed as a percentage. The blue line in the figure, for the direct pressure differences, seems to indicate the rapid breakdown of linearity with increasing perturbation magnitude. A sound speed change of just 10 m/s causes an apparent 100% error in the estimate produced by the kernel, which would severely limit the usability of this approximation. However, given the similarity of the curves in the 10 m/s example in Fig. 2.3, it is reasonable to believe that some linearity remains, despite the calculated 100% error. The primary difference between the two time-series is a slight time-lag/phase-offset, which from a strict pressure-time analysis results in the large error seen in Fig. 2.4, while the envelopes of the signals still appear to be quite similar.

The magnitude and phase differences can be separated through demodulation of the pressure-time series (complex basebanding with $e^{-i\omega_c t}$, where ω_c is the center/carrier frequency). Repeating the error analysis with these demodulated quantities yields a far more appealing picture, the green line in Fig. 2.4, with the RMS error in magnitude staying below 50% even as the perturbation scale approaches 20 m/s, at which point the error in the direct pressure signal is over 400%. With this observation it appears prudent to transform the PSK into equivalent phase and magnitude counterparts as well, as described in Sec. 2.2.2, that can

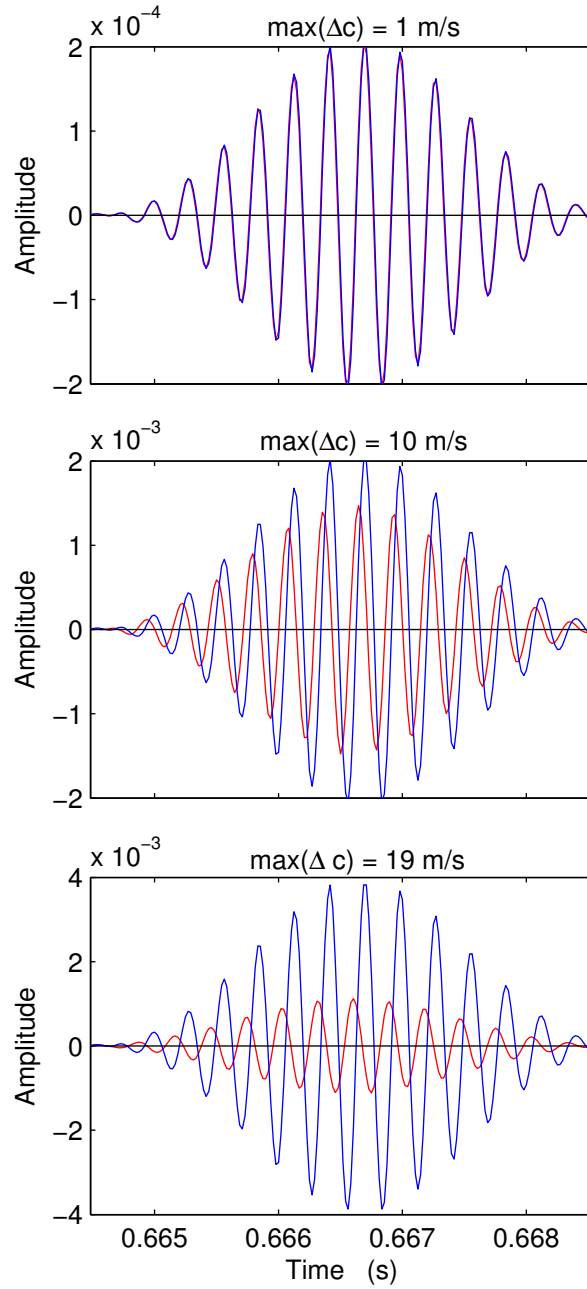


Figure 2.3: These 3 graphs plot $\Delta \hat{p}(t)$ (blue) and $\Delta p(t)$ (red) on the same time-base, for increasing values of $\max(\Delta c)$. The time window encompasses the pulse-width of arrival #1 in Fig. 2.1b to show the linear increase in the kernel estimate ($\Delta \hat{p}(t)$) vs the actual. Note the change in scale for the amplitude (vertical) axis, moving from the first (top) panel down.

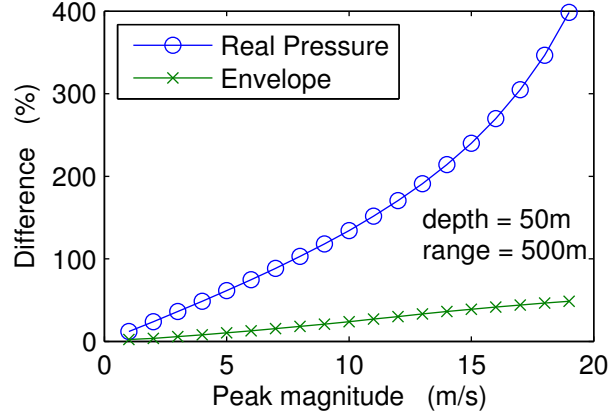


Figure 2.4: RMS differences between the kernel estimate, $\Delta\hat{p}(t)$, and the direct simulated change, $\Delta p(t)$, for increasing values of $\max(\Delta c)$, where the mean is taken across the whole signal. This provides a quantitative view of the divergence seen in Fig. 2.3, but across the entire time series, and also shows the benefit of working with the envelope of the signal.

then be treated independently. Further tests were conducted to explore the range of linearity for these phase and magnitude sensitivity kernels (PhSK, MSK), and the results for one particular isolated peak (arrival #3) are presented in Fig. 2.5. Here, the linear increases predicted by the sensitivity kernels can be clearly seen, but quickly deviate from the truth for the raw pressure example, where only the first point (at 1m/s) matches the perturbed PE output

2.3.2 Information content

In the previous section, it was shown that perturbations to a received broadband pressure signal have a larger linear range when demodulated into separate magnitude and phase components. The broadband PSK can be correspondingly transformed into magnitude and phase analogues as well, but is not simply the complex demodulation of the real pressure kernel. The formulations for sensitivity of magnitude and phase are given by Eq. (2.8) and Eq. (2.9), respectively. Both of these kernels are easily calculated given the existence of the base sensitivity computation from Eq. (2.7), as shown in Sec. 2.2.2.

Figures 2.6a and 2.6b present the magnitude and phase kernels, respectively,

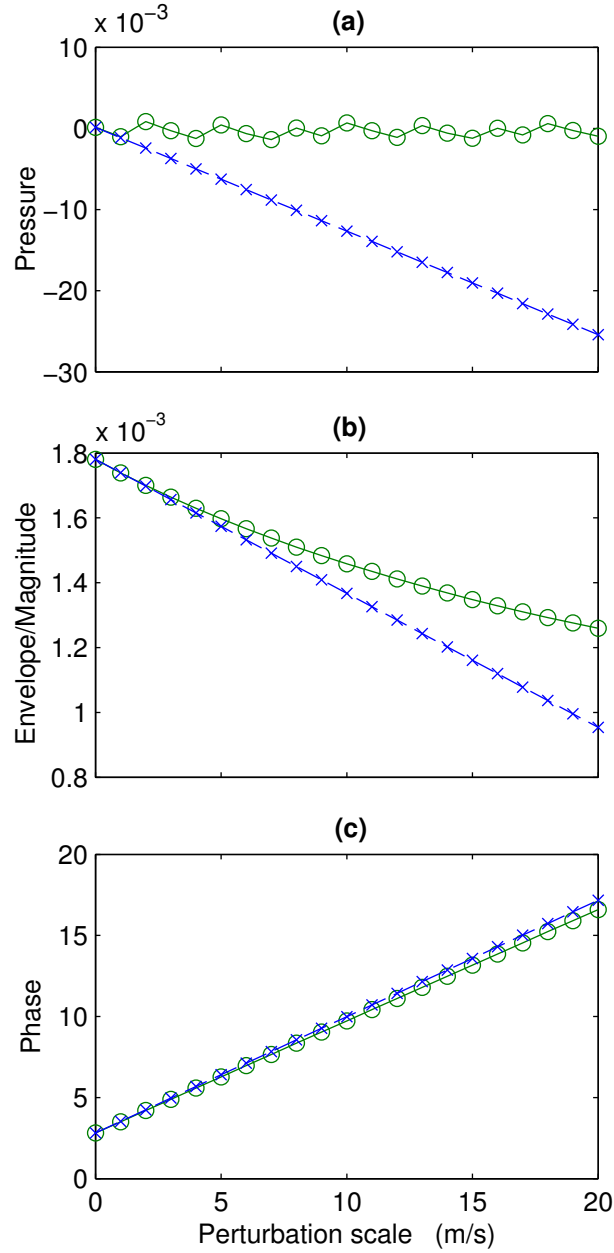


Figure 2.5: The evolution of peak arrival #3 (in Fig. 2.1) as the scale of a gaussian perturbation in the center of the environment is increased. The green lines, with circular markers, plot the perturbed PE results while the blue lines, with cross markers, indicate the linear kernel estimated changes. Panel (a) presents the changes in the raw pressure value at arrival #3, and its associated kernel. Panels (b) and (c) show the equivalent results for the demodulated (envelope) magnitude and phase quantities, respectively. Note, in panel (a) the perturbed PE output oscillates around the 0-line as the wave-packet within the peak shifts, but this is obscured by how much the raw pressure kernel overestimates the changes.

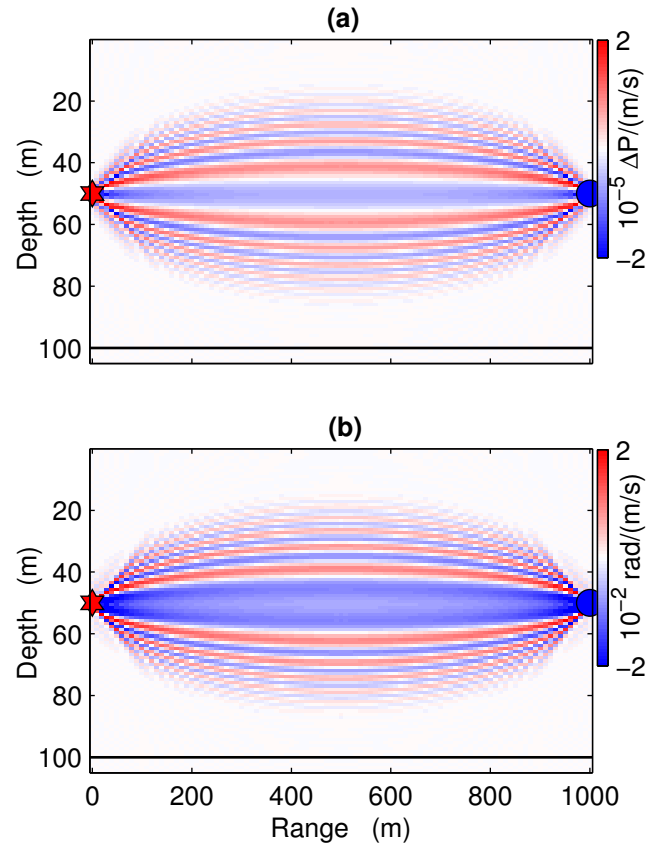


Figure 2.6: Sensitivity kernels for envelope/amplitude (a) and phase (b), for arrival 1 as marked in Fig. 2.1b

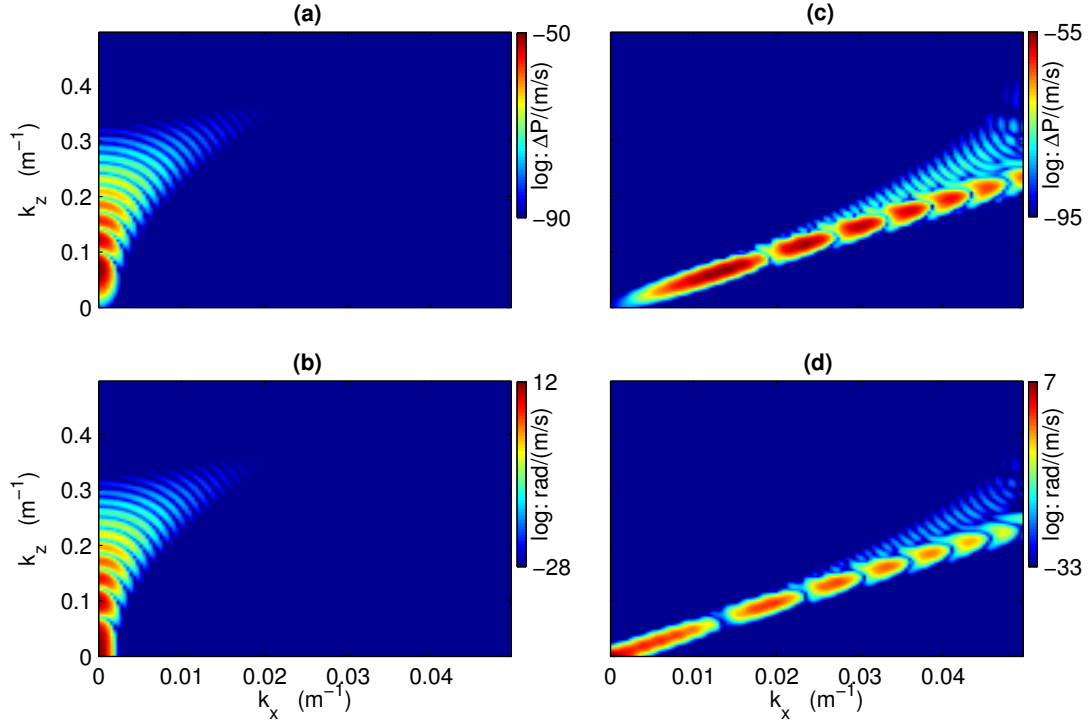


Figure 2.7: Panels (a) and (b) show the 2D spatial Fourier transforms of the magnitude and phase kernels, respectively, given in Fig. 2.6 for arrival #1. Panels (c) and (d) are the equivalent spectrums for arrival #3 in Fig. 2.1b. The color values describe a logarithmic scale ($20 \log_{10}$) for the magnitude of the FFT output, to compress the dynamic range of the visible features, and do not represent a power-spectral density (PSD).

for arrival #1 in Fig. 2.1b. The phase kernel is analogous to the TSK[7] for small perturbations, since travel-time and phase are linearly related, so the important question is whether the magnitude provides any further information about the environment over travel-time/phase alone. At first glance it is difficult to discern any significant differences between the two maps, aside from the width of the central lobe. Closer inspection of the phase kernel reveals fading in the main lobe towards the central axis, i.e. the eigenray path for this arrival. In contrast, the magnitude kernel has a solid main-lobe, indicating non-zero sensitivity along the ray- path. This behavior was observed in three dimensions for amplitude kernels calculated on seismic body waves by Dahlen.[26]

Given these differences between the magnitude and phase kernels, it is nat-

ural to examine them out in the higher Fresnel zones. Calculating the 2D spatial Fourier transform of each kernel provides a measure of their sensitivities to different scales of variability within the environment, as shown in Fig. 2.7. The most prominent feature of these spectra is that the phase appears maximally sensitive to the (0,0) wavenumber, whereas the magnitude has no sensitivity at all there. This meshes well with our intuition of the problem: the (0,0) wavenumber corresponds to a uniform increase (or decrease) in sound speed over the whole environment, and such a change would serve to only accelerate (or retard) the existing arrival structure and have no effect on the amplitude of the peaks. Examining the rest of the spectrum, it is apparent that both amplitude and phase are only sensitive to low horizontal wavenumbers because of the horizontally stratified character of the spatial sensitivity maps for this particular (direct) path - any higher frequency variability is integrated out during propagation.

Following the vertical structure of both spectra, an interesting feature stands out: the maximal and minimal sensitivities of the two kernels appear to be interleaved. Besides the already discussed (0,0) difference between the two, the phase spectrum has local maxima at 0.1 m^{-1} and 0.2 m^{-1} in the vertical, whereas the amplitude kernel has local minima at those points. This relationship is even more apparent for the later (high angle) arrivals, where the spatial spectrum is more separated. Figures 2.7c and 2.7d show the Fourier transforms of the magnitude and phase kernels associated with arrival #3 in Fig. 2.1b, and one can clearly discern the alternating minima/maxima between the two spectra. The corresponding spatial maps in amplitude and phase have not been provided, but are similar in appearance to Fig. 2.2c, the main differences lying in the fine structure. Other than the argument given above for the lowest (flat) wavenumber, the physical reason behind this apparent interleaving has not been determined.

2.4 Inverting for sound speed changes

In this section, a standard least-squares method is used to simultaneously invert magnitude and phase/time information for sound-speed perturbations using

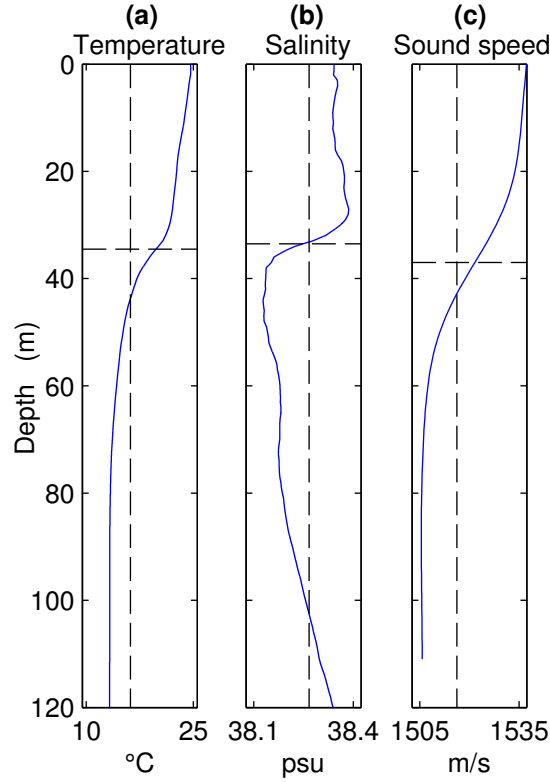


Figure 2.8: FAF05 profiles for temperature (a), salinity (b) and sound speed (c) showing mean (vertical dashed line) and thermocline (horizontal dashed line). These profiles are the average of several CTD casts, and the resulting sound speed profile has been smoothed prior to use in numerical simulations.

the sensitivity kernels discussed above.

The Pekeris waveguide used earlier is now replaced by a range-independent summer profile derived from CTD measurements (Fig. 2.8) taken during the Focused Acoustic Fields experiments of 2005 (FAF05) through which the reference data model is constructed, along with the related sensitivity kernels. To increase coverage over the medium, we allow for multiple sources and receivers (10x10) spanning the water column (now 120 m deep), an idealization of the at-sea experimental setups, which had 29 sources and 32 receivers.

To generate realistic perturbations, an internal-wave model is constructed using the same CTD measurements. The vertical basis functions of the internal-wave field are estimated from the buoyancy profile derived from the FAF05 environmental data, while the horizontal basis functions are sines and cosines[27].

The spectrum employed in weighting these components is the Garret-Munk (GM) spectrum[28], but rescaled to produce the desired range of variability (± 1.0 m/s at the thermocline, which is ~ 35 m deep).

In vector notation, the forward problem is described by

$$\Delta \mathbf{p} = \frac{\partial \mathbf{p}}{\partial \mathbf{c}} \Delta \mathbf{c},$$

where $\Delta \mathbf{c}$ is the sound speed perturbation expressed as a column vector, of length $N_x N_z$ - where N_x and N_z are the number of grid points in the horizontal, and vertical spatial dimensions, respectively. $\frac{\partial \mathbf{p}}{\partial \mathbf{c}}$ is a Jacobian matrix or sensitivity kernel expressed as a row vector of the same size, and $\Delta \mathbf{p}$ is the resulting change in pressure (or magnitude and phase) at the peak arrival. This relationship provides two data points when considering the demodulated quantities for magnitude and phase (each with their own kernel), and every peak in the arrival structure provides a pair of such values. The data vector is expanded with each source-receiver pair, and the entire system can now be expressed concisely by

$$\mathbf{d} = \mathbf{H} \Delta \mathbf{c},$$

where $\Delta \mathbf{c}$ is as before; \mathbf{d} is the perturbed data vector (length N_d) - the differences between our measurements - combining all amplitude and phase points for each peak-arrival in every source-receiver pair; and \mathbf{H} is a matrix whose rows consist of sensitivity kernels for all the peaks under consideration (size $N_d \times N_x N_z$). In the simulations presented here, the average number of peaks for each time-series is 6, so that the number of data points, N_d , is ~ 1200 ($10 \times 10 \times 6 \times 2$). An estimate of the sound speed perturbation is now given by

$$\widehat{\Delta \mathbf{c}} = \mathbf{H}^+ \mathbf{d},$$

where \mathbf{H}^+ is the Gauss-Markov inverse, as detailed in the appendix. The number of unknowns in this system is governed by the grid size employed during the PE calculations ($N_x = 201, N_z = 2801$); resulting in over 500,000 variables to be determined from just 1200 equations - a severely under-determined situation. The specification of the prior covariance can be diagonalized by projecting onto the

physical basis functions used by the internal-wave model mentioned above. The set of sensitivity kernels are transformed into this basis function space producing a new matrix,

$$\mathbf{H}' = \mathbf{H}\mathbf{M},$$

where each column of the matrix \mathbf{M} is an orthonormal product of basis functions from the internal-wave model, and may be restricted to as few (or as many) functions as needed, depending upon desired spatial resolution. The inversion process now produces an estimate of the coefficients of these basis functions that constitute the sound speed perturbation:

$$\widehat{\Delta \mathbf{m}} = \mathbf{H}'^+ \mathbf{d}.$$

The spatial answer can then be reconstructed by

$$\widehat{\Delta \mathbf{c}} = \mathbf{M} \widehat{\Delta \mathbf{m}}.$$

The actual inversion step incorporates the statistics of the internal-wave model, as well as an assumption about the statistics of the expected misfit between the model and the observations. This is called “noise”, and is used to tune the performance of the estimate:

$$\mathbf{H}'^+ = \mathbf{C} \mathbf{H}'^T (\mathbf{H}' \mathbf{C} \mathbf{H}'^T + \mathbf{R})^{-1}. \quad (2.11)$$

\mathbf{C} is a diagonal covariance matrix for the internal wave parameters that conditions the estimate based on expected energies of the internal wave modes; and the diagonal matrix \mathbf{R} is the variance of the expected misfit between the model and the observations. The uncertainty in the estimated sound-speed can be calculated by

$$\begin{aligned} \widehat{\mathbf{C}} &= \left\langle (\widehat{\Delta \mathbf{c}} - \Delta \mathbf{c})(\widehat{\Delta \mathbf{c}} - \Delta \mathbf{c})^T \right\rangle \\ &= \mathbf{C} - \mathbf{C} \mathbf{H}'^T (\mathbf{H}' \mathbf{C} \mathbf{H}'^T + \mathbf{R})^{-1} \mathbf{H}' \mathbf{C}. \end{aligned}$$

2.4.1 Numerical example

The perturbation map shown in Fig. 2.9a is a randomly generated instance of the internal-wave field described earlier, using 10 vertical and 80 horizontal components. The PE simulation is calculated through this perturbed environment (as

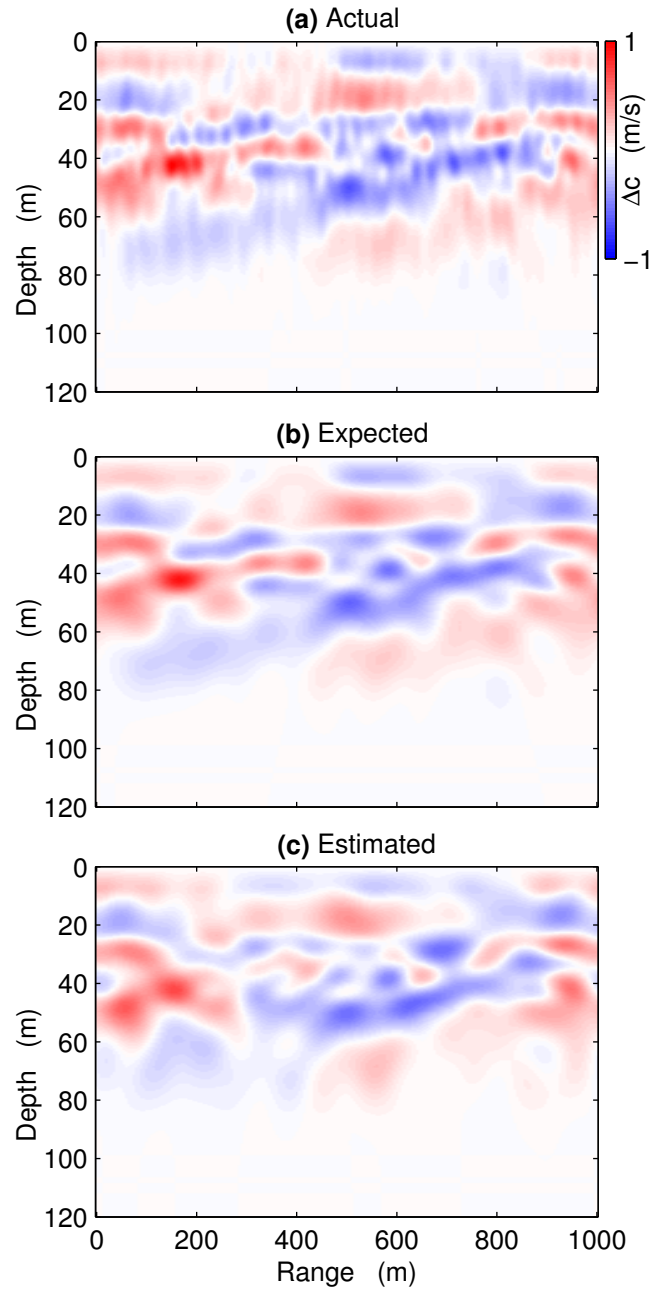


Figure 2.9: (a): Sound speed perturbation map used to generate data. Constructed with 10 vertical internal wave modes and 80 horizontal functions (800 total components).

(b): Expected perturbation field when limited to the 20 largest horizontal modes.

(c): Inversion result for the perturbation field, using both complex demodulated amplitude and phase data. The estimation process utilized all 10 vertical modes, but limited to the first 20 horizontal functions - 200 total unknowns to determine.

in Sec. 2.3.1), and a peak finding algorithm applied to the resulting pressure-time series to identify arrivals and associate them with counterparts in the unperturbed model. The differences in amplitude and phase provide the elements of the data vector d . As part of the peak identification process an eigenray search is performed to assist in match-making. In some cases, like arrivals 2 and 3 in Fig. 2.2, a peak can be associated with more than one ray-path. Such data points are discarded because the resulting constructive/destructive interference reduces the range of linearity of the amplitude and phases kernels to that of the full wave pressure kernel. Another source of non-linearity is propagation paths with turning points close to the thermocline: these rays are easily deviated from their original travel paths, with even small changes in sound speed. A substantial path change equates to a new kernel structure as well, and hence the original sensitivity calculation will no longer be valid. However, this behavior tends to be highly dependent on the actual structure of the perturbation, making identification of individual problem-paths difficult a priori. In these numerical examples all the 1st (direct) arrivals have been removed, as these shallow rays appear to be particularly prone to small ranges of linearity.

These two filtering steps result in about 50% of the initial data points being discarded.

Figure 2.9c shows the results of the estimation using all acceptable data points (amplitude and phase) with an assumed signal-to-noise ratio (SNR) of 35 dB, but only allowing for the first 20 most significant horizontal components while keeping all 10 vertical modes. The resulting map of sound speed deviations should be compared to the original input, Fig. 2.9a. The estimate appears to be a smoother, filtered version of the original - expected, due to the exclusion (truncation) of high wavenumbers - but with most of the main structures intact. When compared directly to a truncated version (Fig. 2.9b) of the input perturbation field, the amount of agreement is even more pronounced. The differences between the estimated and true perturbations were consistent with the diagonal of the *a posteriori* uncertainty covariance matrix of the estimate. This is expected for a simulation with inputs consistent with the *a priori* assumptions and so the

expected uncertainty map has been omitted.

This inversion can be performed with phase and amplitude data separately or combined, and the quality of the estimate varies accordingly. Figure 2.10a, shows the error in the estimate for all 3 cases vs. varying values of assumed SNR, which increases the diagonal loading applied through the matrix R (Eq. 2.11). The performance of the estimator decreases at high SNR due to non-linearity, as the assumed noise level is now less than the actual. Here we can see that even though phase alone fares substantially better than amplitude inversions, combined the resulting estimate provides even more information. Figure 2.10b shows a similar plot of error vs. the number of horizontal components inverted for - keeping the SNR constant at 35 dB. This graphically shows the motivation for limiting the estimation to the 200 most significant basis functions (out of the original 800): searching for any higher-order structure yields little-to-no improvement in the final answer, which is also supported by the observations from Fig. 2.7. The dashed lines represent the ideal cases (with respect to the sensitivity kernels), i.e. if the data vectors had been generated with the kernels themselves through Eq. (2.10). These curves represent the best possible cases when every data-point used falls within the linear regime.

2.5 Discussion and Conclusions

Application of the Born approximation to the wave equation provides a linear relationship between sound speed fluctuations and changes in received pressure. This association is a function of frequency, but can be converted into a time-dependent pressure sensitivity kernel via the Fourier transform. These spatial sensitivity kernels map out the areas of the environment that affect the acoustic signal, and at high frequencies approach the assumed ray/beam paths normally associated with propagation. Numerically, they quantify the effect environmental changes have on the received pressure, but only to the extent that the assumption of linearity permits.

We explored the extent of this linear limit, noting that the raw pressure

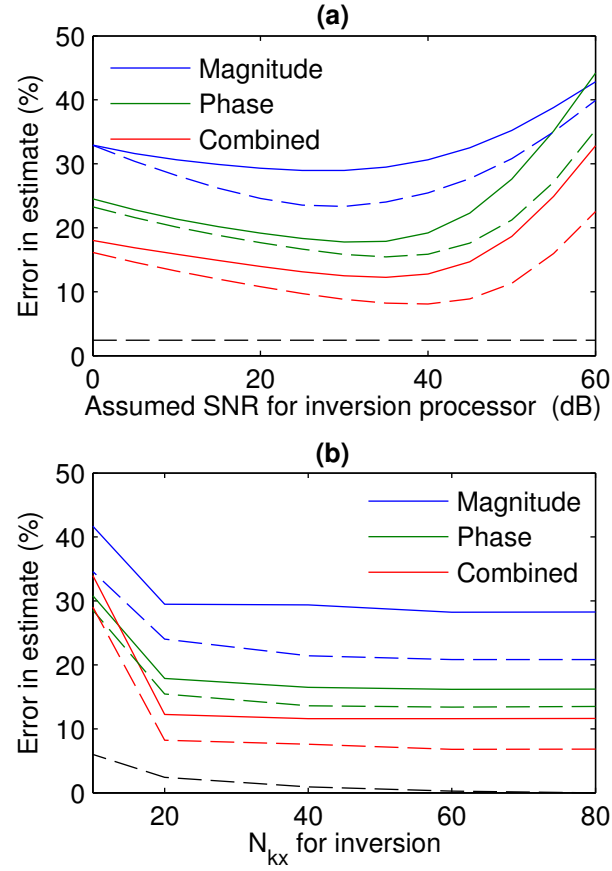


Figure 2.10: Error in inversion estimate vs. assumed SNR ($N_{kx} = 20$) (a), and # of horizontal components (b). Solid lines describe the estimation with data generated via the perturbed PE model; dashed lines are the kernels self-reflected output, i.e. best case. The error value is determined via a 0,0 lag 2D correlation coefficient of the actual and estimated sound speed perturbation maps. The broken black line in both plots, indicates the loss of information expected from the reduced spatial component set alone.

signal becomes non-linear very quickly, while the demodulated pulse envelope phase and magnitude stay in the linear regime far longer. With this in mind we transform the PSK into equivalent linear magnitude and phase kernels, and note that phase sensitivity should be similar to earlier work done on travel-time perturbations. The character of the additional information provided by the inclusion of magnitude data is explicitly shown by the spatial Fourier transforms of the kernel maps. We see that phase and magnitude data are not only complementary, but may also be mutually exclusive (at least in the spectral sense).

Using these kernels for inversions requires prior estimates for the statistics of the sound speed perturbations. Limiting the degrees of environmental variability to known physical modes, via an internal-wave model, leads to a convenient and diagonal prior uncertainty covariance.

A numerical example of inverting for sound speed changes with these sensitivity kernels was performed using simulated data created by propagating sound through a sound speed field produced by an internal-wave model. The resulting estimate shows good agreement when compared to the input perturbation map. The inversion was performed with phase and magnitude data separately, as well as combined, and shows the benefit of including full-wave data (when possible) for inversions.

2.A Adjoints, kernels, and inverse techniques

This discussion assumes linearity in order to focus on the linear algebra of the adjoint, kernel, and inverse problems. Using the notation from Sec. 2.4, the linearized forward problem is written in matrix notation as

$$\mathbf{d} = \mathbf{H}\Delta\mathbf{c} + \mathbf{r},$$

where $\Delta\mathbf{c}$ is the sound speed perturbation expressed as a vector (length $N_x N_z$), \mathbf{d} is a data vector (length N_d) combining all amplitude and phase observations, \mathbf{r} is a vector of misfit between observations and model with an expected covariance \mathbf{R} , and \mathbf{H} is the $N_d \times N_x N_z$ jacobian matrix that converts sound speed-perturbations

to data-perturbations. Each row of \mathbf{H} is the sensitivity kernel for the corresponding datum.

Kernels can be estimated using the Born approximation or by the adjoint of the forward model, although the latter has typically been used for iterative inversion without explicitly evaluating the kernels. To use the adjoint for inversions, the cost function for the differences between observation and model,

$$\mathbf{J} = (\mathbf{d} - \mathbf{H}\Delta\mathbf{c})^T \mathbf{R}^{-1}(\mathbf{d} - \mathbf{H}\Delta\mathbf{c}),$$

is differentiated with respect to the unknown, $\Delta\mathbf{c}$ to get

$$\frac{\partial \mathbf{J}}{\partial \mathbf{c}} = -2\mathbf{H}^T \mathbf{R}^{-1}(\mathbf{d} - \mathbf{H}\Delta\mathbf{c}).$$

\mathbf{H}^T is the adjoint of the forward model, and the gradient $\frac{\partial \mathbf{J}}{\partial \mathbf{c}}$ can be used in an iterative descent method (e.g. conjugate gradients) to minimize \mathbf{J} . The adjoint-based ocean estimation has been done this way ,[16, 18, 19] where the adjoint model is forced by the weighted data misfit, $\mathbf{R}^{-1}(\mathbf{d} - \mathbf{H}\Delta\mathbf{c})$.

If the model is instead forced by a single datum, the gradient is $\mathbf{H}^T \mathbf{e}_i$, where \mathbf{e}_i is the vector basis function with the i -th element equal to 1 and all other elements zero. This selects one column of \mathbf{H}^T , which is one row of \mathbf{H} , the same as the kernel derived above. This matrix is frequently too large to compute, and so the iterative gradient descent is used in order to work with only one set of vectors ($\Delta\mathbf{c}$, $\frac{\partial \mathbf{J}}{\partial \mathbf{c}}$ and $(\mathbf{d} - \mathbf{H}\Delta\mathbf{c})$) at a time.

In systems where the number of data or model parameters are small enough, sound speed can be estimated without iteration by inverting a matrix. To deal with the possibility that \mathbf{H} is poorly conditioned, and/or to satisfy prior constraints in Bayesian estimation, the cost function is expanded to include a penalty on the size and/or roughness of $\Delta\mathbf{c}$:

$$\mathbf{J} = (\mathbf{d} - \mathbf{H}\Delta\mathbf{c})^T \mathbf{R}^{-1}(\mathbf{d} - \mathbf{H}\Delta\mathbf{c}) + \Delta\mathbf{c}^T \mathbf{C}_c^{-1} \Delta\mathbf{c},$$

where \mathbf{C}_c is a matrix defining the penalty for structure in $\Delta\mathbf{c}$, which Bayesians interpret as the expected covariance of the uncertainty in the initial sound speed guess (for which $\Delta\mathbf{c}$ is a correction). The transformation to internal wave parameters is not used here to simplify the discussion.

Now the cost function gradient has an extra term:

$$\frac{\partial J}{\partial \mathbf{c}} = -2\mathbf{H}^T \mathbf{R}^{-1}(\mathbf{d} - \mathbf{H}\Delta\mathbf{c}) + 2\mathbf{C}^{-1}\Delta\mathbf{c}$$

. The solution minimizes the cost function, so the gradient is zero, so

$$\mathbf{H}^T \mathbf{R}^{-1}(\mathbf{d} - \mathbf{H}\Delta\mathbf{c}) = \mathbf{C}_c^{-1}\Delta\mathbf{c}$$

or

$$\mathbf{H}^T \mathbf{R}^{-1}\mathbf{d} = (\mathbf{H}^T \mathbf{R}^{-1}\mathbf{H} + \mathbf{C}_c^{-1})\Delta\mathbf{c}.$$

This matrix problem can be inverted iteratively, using the cost function gradient, but it can also be formally inverted:

$$\widehat{\Delta\mathbf{c}} = (\mathbf{H}^T \mathbf{R}^{-1}\mathbf{H} + \mathbf{C}_c^{-1})^{-1}\mathbf{H}^T \mathbf{R}^{-1}\mathbf{d}.$$

The matrix to be inverted is called the ‘‘Hessian’’ and is $N_x N_z \times N_x N_z$. Frequently, as in this paper, this matrix is far too large to even compute, let alone invert, but if the number of data are small, the matrix inversion lemma (for example, see Wunsch[29]) gives an equivalent form which can be inverted in data space:

$$\widehat{\Delta\mathbf{c}} = \mathbf{C}_c \mathbf{H}^T (\mathbf{H} \mathbf{C}_c \mathbf{H}^T + \mathbf{R})^{-1} \mathbf{d}.$$

This is the Gauss-Markov estimator used in Sec. 2.4, and is numerically feasible if N_d is small enough. So the adjoint can be used for gradient descent in large problems, or to generate kernels for individual observations.

Acknowledgements

The text of this chapter is, in full, a reprint of material published in *The Journal of the Acoustical Society of America*: Jit Sarkar, Bruce D. Cornuelle, and William A. Kuperman, ‘‘Information and linearity of time-domain, complex-demodulated, amplitude and phase data in shallow water’’. The dissertation author was the primary investigator and author of this paper.

References

- [1] Walter H Munk and Carl Wunsch. Ocean acoustic tomography: a scheme for large scale monitoring. *Deep-Sea Res.*, 26(1):23–1, 1979.
- [2] Walter H. Munk, Peter F. Worcester, and Carl Wunsch. *Ocean acoustic tomography*, chapter 5. Cambridge University Press, Cambridge; New York, 1995.
- [3] Walter H Munk and Carl Wunsch. Ocean acoustic tomography: Rays and modes. *Rev. Geophys. Space Phys.*, 21(4):777–793, Jan 1983.
- [4] E C Shang. Ocean acoustic tomography based on adiabatic mode theory. *J. Acoust. Soc. Am.*, 85(4):1531–1537, 1989.
- [5] Gerassimos A Athanassoulis and Emmanuel K Skarsoulis. Arrival-time perturbations of broadband tomographic signals due to sound-speed disturbances. a wave-theoretic approach. *J. Acoust. Soc. Am.*, 97(6):3575–3588, 1995.
- [6] Emmanuel K Skarsoulis, Gerassimos A Athanassoulis, and Uwe Send. Ocean acoustic tomography based on peak arrivals. *J. Acoust. Soc. Am.*, 100(2):797–813, 1996.
- [7] Emmanuel K Skarsoulis and Bruce D Cornuelle. Travel-time sensitivity kernels in ocean acoustic tomography. *J. Acoust. Soc. Am.*, 116(1):227–238, 2004.
- [8] F A Dahlen, S H Hung, and Guust Nolet. Fréchet kernels for finite-frequency traveltimes-I. theory. *Geophys. J. Int.*, 141(1):157–174, 2000.
- [9] Jeroen Tromp, Carl Tape, and Qinya Liu. Seismic tomography, adjoint methods, time reversal and banana-doughnut kernels. *Geophys. J. Int.*, 160(1):195–216, Jan 2005.
- [10] Ion Iturbe, Philippe Roux, Jean Virieux, and Barbara Nicolas. Travel-time sensitivity kernels versus diffraction patterns obtained through double beam-forming in shallow water. *J. Acoust. Soc. Am.*, 126(2):713–720, Jan 2009.
- [11] Michael D Collins, William A Kuperman, and Henrik Schmidt. Nonlinear inversion for ocean-bottom properties. *J. Acoust. Soc. Am.*, 92(5):2770–2783, Jan 1992.
- [12] Olivier Carrière, Jean-Pierre Hermand, Jean-Claude Le Gac, and Michel Rixen. Full-field tomography and Kalman tracking of the range-dependent sound speed field in a coastal water environment. *J. Marine Syst.*, 78:S382–S392, Jan 2009.

- [13] Peter Gerstoft. Inversion of seismoacoustic data using genetic algorithms and a posteriori probability distributions. *J. Acoust. Soc. Am.*, 95(2):770–782, Jan 1994.
- [14] Stephen J Norton. The inverse-scattering problem and global convergence. *J. Acoust. Soc. Am.*, 118(3):1534–1539, 2005.
- [15] Stan E Dosso and Jan Dettmer. Bayesian matched-field geoacoustic inversion. *Inverse Problems*, 27(5):055009, 2011.
- [16] Paul Hursky, Michael B Porter, Bruce D Cornuelle, William S Hodgkiss, and William A Kuperman. Adjoint modeling for acoustic inversion. *J. Acoust. Soc. Am.*, 115(2):607–619, 2004.
- [17] Aaron M Thode. The derivative of a waveguide acoustic field with respect to a three-dimensional sound speed perturbation. *J. Acoust. Soc. Am.*, 115(6):2824–2833, Jan 2004.
- [18] Jean-Pierre Hermand, Matthias Meyer, Mark Asch, and Mohamed Berrada. Adjoint-based acoustic inversion for the physical characterization of a shallow water environment. *J. Acoust. Soc. Am.*, 119(6):3860–3871, 2006.
- [19] Matthias Meyer, Jean-Pierre Hermand, Mark Asch, Jean-Claude Le Gac, and Den Helder. An analytic multiple frequency adjoint-based inversion algorithm for parabolic-type approximations in ocean acoustics. *Inverse Probl. Sci. En.*, 14(3):245–265, Jan 2006.
- [20] Stephen J Norton. Iterative inverse scattering algorithms: Methods of computing Fréchet derivatives. *J. Acoust. Soc. Am.*, 106(5):2653–2660, 1999.
- [21] Ion Iturbe, Philippe Roux, Barbara Nicolas, Jean Virieux, and Jérôme I Mars. Shallow-water acoustic tomography performed from a double-beamforming algorithm: Simulation results. *IEEE J. Oceanic Eng.*, 34(2):140–148, Jan 2009.
- [22] Kaustubha Raghukumar, Bruce D Cornuelle, William S Hodgkiss, and William A Kuperman. Pressure sensitivity kernels applied to time-reversal acoustics. *J. Acoust. Soc. Am.*, 124(1):98–112, Jan 2008.
- [23] F. B. Jensen, W. A. Kuperman, M. B. Porter, and H. Schmidt. *Computational ocean acoustics*, chapter 2.3.3. American Institute of Physics, Woodbury, NY, 1994.
- [24] Max Born. The quantum mechanics of the impact process. *Z. Phys*, 37(12):863–867, Jan 1926.

- [25] Michael D Collins. Applications and time-domain solution of higher-order parabolic equations in underwater acoustics. *J. Acoust. Soc. Am.*, 86(3):1097–1102, Jan 1989.
- [26] F A Dahlen and Adam M Baig. Fréchet kernels for body-wave amplitudes. *Geophys. J. Int.*, 150(2):440–466, 2002.
- [27] John A Colosi and Michael G Brown. Efficient numerical simulation of stochastic internal-wave-induced sound-speed perturbation fields. *J. Acoust. Soc. Am.*, 103(4):2232–2235, Jan 1998.
- [28] Christopher Garrett and Walter H Munk. Space-time scales of internal waves: A progress report. *J. Geophys. Res.*, 80(3):291–297, Jan 1975.
- [29] C. Wunsch. *The Ocean Circulation Inverse Problem*, chapter 3.1. Cambridge University Press, New York, 1996.

Chapter 3

The phase sensitivity kernel and its performance as a linear travel-time estimator

Abstract

Linear acoustic sensitivity kernels have been derived for the pressure, arrival-time, complex amplitude and phase of broadband acoustic transmissions. While the additional information provided by amplitude data has been previously investigated, it was assumed that phase could be directly related to travel-time measurements, and hence yielded no new details. Further investigation shows that this is not always the case, and that the kernel framework suggests certain situations where phase and time diverge, which is also supported by perturbed forward simulations. This paper presents several such examples from short-range numerical models, along with a statistical analysis investigating the performance of amplitude, phase and travel-time sensitivity kernels as linear acoustic estimators. The results suggest phase may be a preferable observable to travel-time, and even when considering travel-time measurements alone, the phase-derived time sensitivity is a better performing estimator.

3.1 Introduction

In ocean acoustic tomography, travel-time has been the observable of choice since being first suggested by Munk and Wunsch[1, 2] to monitor basin-scale changes. This was a ray-centric approach to relating measured acoustic perturbations to changes in ocean sound-speed, but rays are an infinite bandwidth approximation to the actual propagation of sound in the ocean, one that while adequate for coarse observations, is inaccurate for resolving finer scales of ocean structure, especially at low frequencies. As an alternative, wave-theoretic approaches have been employed, such as the modal-arrival[3, 4] and the peak arrival approach[5, 6], which led to the development of the Travel-time Sensitivity Kernel (TSK)[7], an application of first-order perturbation theory to the effects of sound-speed fluctuations in the wave equation. TSK analysis, and previous seismological literature[8, 9], moved away from the high-frequency assumption to provide a wave-theoretic relation between a time-of-arrival and the parts of the medium that affect it.

This sensitivity analysis has been extended to include both the amplitude and phase of a peak-arrival, and not just its observed travel-time. It was presumed that the instantaneous phase could be directly related to travel-time measurements, and hence provided no additional information, while amplitude was shown to carry additional data about the medium over that indicated in the phase sensitivity kernels alone.

In the current work, all three kernel types - amplitude, phase and time - are explored further via extensive linearity tests against perturbed numerical forward models. These tests are performed in detail, to probe the behavior of the acoustics in specific examples, and in aggregate, to describe how well the sensitivity kernels perform as general linear estimators. The phase and time sensitivity kernels in particular are compared in an attempt to reconcile the two related quantities.

Section 3.2 begins by summarizing the math for the three sensitivity kernels noted above. In Sec. 3.2, the testing methods used to probe the linearity and performance of each kernel are described, followed by a discussion of a few specific example results for a summer-type profile in Sec. 3.3. The differences between phase and travel-time estimates are explored in more detail within Sec. 3.3.3,

and the performance of the sensitivity kernels are summarized statistically during Sec. 3.3.4. Finally, Sec. 3.4 contains a discussion of the results and main conclusions from this work.

3.2 The sensitivity kernel equations

The detailed derivations for each of the sensitivity kernels are provided in earlier work[7], and are only presented in summary here.

In the following inhomogeneous Helmholtz equation, the Green's function $G(\mathbf{r}|\mathbf{r}_s)$ represents the acoustic pressure field response at a position \mathbf{r} , due to a point source located at \mathbf{r}_s :

$$\left[\nabla^2 + \frac{\omega^2}{c^2(\mathbf{r})} \right] G(\mathbf{r}|\mathbf{r}_s) = -\delta(\mathbf{r} - \mathbf{r}_s). \quad (3.1)$$

Here, ω is the circular frequency of the source, $c(\mathbf{r})$ describes the sound-speed distribution, and δ is the Dirac delta-function. Introducing a sound-speed perturbation of Δc will induce a corresponding change in the Green's function of ΔG . Expanding this expression and linearizing (keeping only first-order terms) produces the the first Born approximation[10]:

$$\frac{\partial G(\mathbf{r}_r|\mathbf{r}_s)}{\partial c(\mathbf{r}')} = -2\omega^2 G(\mathbf{r}'|\mathbf{r}_s) G(\mathbf{r}_r|\mathbf{r}') \frac{1}{c^3(\mathbf{r}')}, \quad (3.2)$$

where \mathbf{r}_r is the location of the receiver, and \mathbf{r}' is an arbitrary point within the medium. The sensitivity for all such points in the region is referred to as the "sensitivity kernel", since the volume integral of the kernel multiplied by a sound-speed perturbation provides the change in the Green's function.

Given the frequency-domain Green's function for propagation to a distant receiver, \mathbf{r}_r , and a source-signal spectrum, $P_s(\omega)$, the acoustic field recorded at the receiver can be expressed through the inverse Fourier transform,

$$p_r(t) = \frac{1}{2\pi} \int_{-\infty}^{\infty} G(\mathbf{r}_r|\mathbf{r}_s; \omega; c) P_s(\omega) e^{i\omega t} d\omega. \quad (3.3)$$

Introducing a perturbation, Δc , as before and simplifying the expression using Eq. 3.2, gives the time-domain expression for sound-speed sensitivity

$$\frac{\partial p_r(t)}{\partial c(\mathbf{r}')} = \frac{1}{2\pi} \int_{-\infty}^{\infty} \left(-2\omega^2 G(\mathbf{r}'|\mathbf{r}_s) G(\mathbf{r}_r|\mathbf{r}') \frac{P_s(\omega)}{c^3(\mathbf{r}')} \right) e^{i\omega t} d\omega. \quad (3.4)$$

The formula in Eq. (3.4) constitutes the primary kernel calculation, which we refer to as the Pressure Sensitivity Kernel (or PSK), and is a necessary component for all the derivative kernels below.

The recorded broadband pressure-signal, $p(t)$, can be demodulated with the central/carrier frequency, ω_c , yielding the complex base-banded signal (appropriately filtered):

$$P(t) = p(t)e^{-i\omega_c t} = v(t) + iw(t).$$

The sensitivity kernel for pressure, $\frac{\partial p}{\partial c}$, may be similarly demodulated:

$$\frac{\partial P}{\partial c} = \frac{\partial p}{\partial c}e^{-i\omega_c t} = \frac{\partial v}{\partial c} + i\frac{\partial w}{\partial c},$$

where the upper-case P is used to represent the complex demodulated quantities; v and w are thus the real and imaginary components respectively. The envelope of the signal is then obtained from the magnitude of P by

$$|P| = \sqrt{v^2 + w^2}.$$

We can now state the definition for the amplitude sensitivity kernel:

$$\frac{\partial |P(t)|}{\partial c(\mathbf{r}')} = \frac{v\frac{\partial v}{\partial c} + w\frac{\partial w}{\partial c}}{\sqrt{v^2 + w^2}}. \quad (3.5)$$

Similarly, the phase of the complex broadband pressure-signal is given by

$$\theta = \tan^{-1} \left(\frac{w}{v} \right),$$

where v and w are as defined above, and θ is the phase in radians. The phase sensitivity is then

$$\frac{\partial \theta(t)}{\partial c(\mathbf{r}')} = \frac{v\frac{\partial w}{\partial c} - w\frac{\partial v}{\partial c}}{v^2 + w^2}. \quad (3.6)$$

Using the same notation, the travel-time sensitivity kernel can be defined as

$$\begin{aligned} \frac{\partial \tau(t)}{\partial c(\mathbf{r}')} = \Re \left\{ \frac{v - iw}{2\pi b} \int_{-\infty}^{+\infty} -i\omega \frac{\partial G}{\partial c} e^{i\omega t} d\omega \right. \\ \left. + \frac{\dot{v} - i\dot{w}}{2\pi b} \int_{-\infty}^{+\infty} -\frac{\partial G}{\partial c} e^{i\omega t} d\omega \right\}, \quad (3.7) \end{aligned}$$

where τ is the unperturbed arrival time of a peak originally identified at time t ; and b is a quantity set as

$$b = \dot{v}^2 + v\ddot{v} + \dot{w}^2 + w\ddot{w},$$

where the overdots denote differentiation with respect to time (double-dot is the 2nd derivative).

At this stage it is interesting to observe that phase changes are assumed to be related to travel-time differences by

$$\Delta\theta = \omega_c \Delta\tau, \quad (3.8)$$

but given the definitions of phase and time sensitivity in Eqs. 3.6 and 3.7, respectively, the transformation of one equation to the other does not appear to be so straightforward, and certainly not just a frequency factor of ω_c inserted somewhere.

Note, that in the sensitivity kernel definitions above (Eqs. 3.5, 3.6 and 3.7), the parameters \mathbf{r}_r , \mathbf{r}_s , \mathbf{r}' and t have been omitted for brevity.

3.3 Linearity and performance tests

In exploring the performance of these kernels as linear estimators for acoustic response to sound-speed perturbations, a parabolic equation (PE) numerical model was employed to compute base range-independent broadband fields - which are used to calculate the sensitivity kernels themselves. PE simulations were also performed through perturbed environments with varying magnitudes of sound-speed displacement, while also estimating the expected changes using the sensitivity kernels, i.e. $\Delta\tilde{d} = \Delta c \frac{\partial d}{\partial c}$, where d is one of the three quantities for which kernels have been calculated.

The base environment is a 1 km wide, 120 m deep channel with no bathymetry (flat bottom). The transmission signal modeled is a broadband pulse ranging from 3 kHz to 4 kHz in frequency, and the resulting acoustic field is sampled at four receiver depths: 15 m, 45 m, 75 m and 105 m. These tests were repeated for the source set at these same depth levels as well.

The sound-speed profile employed as part of this investigation is a smooth summer profile derived from average CTD casts (Fig. 3.2) during the Focused Acoustic Fields Experiment of 2005 (FAF05). Figure 3.1 displays the end-field acoustic results for this summer example. The individual pressure-time series (envelope) for each receiver depth has been included with all significant peak-arrivals identified and marked. Each of these peaks will serve as an observable quantity that is tracked in the tests described below, and the three sensitivity kernels are calculated between the source and each receiver for every peak.

Using this prescribed environment, three different perturbation types are explored for the kernel performance review. Firstly, a uniform sound-speed change over the whole environment is applied. Second, a Gaussian displacement is set in the middle of the water-column, midway between the source and receivers in range. Lastly, a realistic ocean state is generated using measured buoyancy parameters and random weightings. These parameters were taken from the FAF05 observations, generating a set of supported vertical displacement modes about the thermocline (~ 35 m deep), while the horizontal components are merely sine and cosine functions. Examples of these sound-speed perturbation maps are provided in Fig. 3.3, with the exception of the flat/uniform type, which is trivial. For all three types, the magnitude of the sound-speed change is varied from 0 to 5 m/s in 0.25 m/s increments, and the linearity tests repeated. In the realistic case this implies a variability of up to ± 5 m/s — representing patches of both positive and negative sound speed displacements.

3.3.1 Test results presentation format

The 4×4 (#sources \times #receivers) array choice results in ~ 100 individual peak-arrivals to observe as the sound-speed profile is perturbed. The discussion here will be limited to the results from just the 45 m source and only a few selected peaks, one from each receiver. Results from all source depths, and all peaks, will be considered in summary for the statistical discussion in Sec. 3.3.4

The figures here aggregate a large amount of information for each peak into individual panels - this was done to keep relevant details together for the

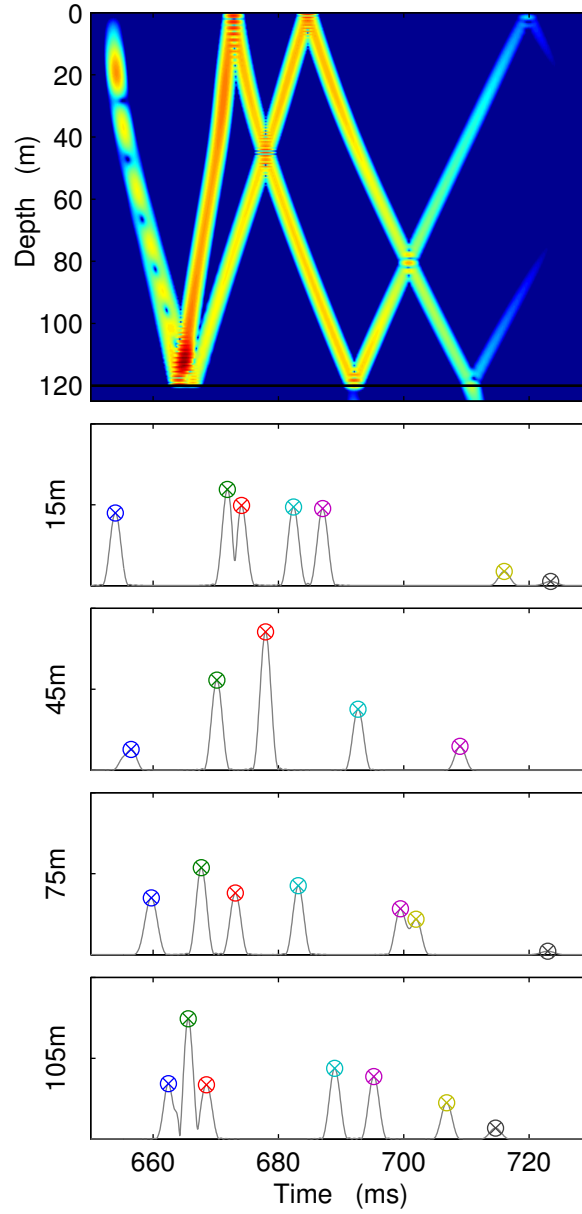


Figure 3.1: Numerical results from a Parabolic Equation (PE) simulation of a 1 km wide, 120 m deep waveguide, using a summer sound-speed profile derived from the FAF05 experiment CTD observations (Fig. 3.2). The top panel shows the arrival structure associated with a source placed 45 m below the surface. The subsequent plots show the individual pressure-time series (complex envelope) from four receiver elements at depths of 15 m, 45 m, 75 m, and 105 m - with significant peaks identified and marked, so that they can be referred to later.

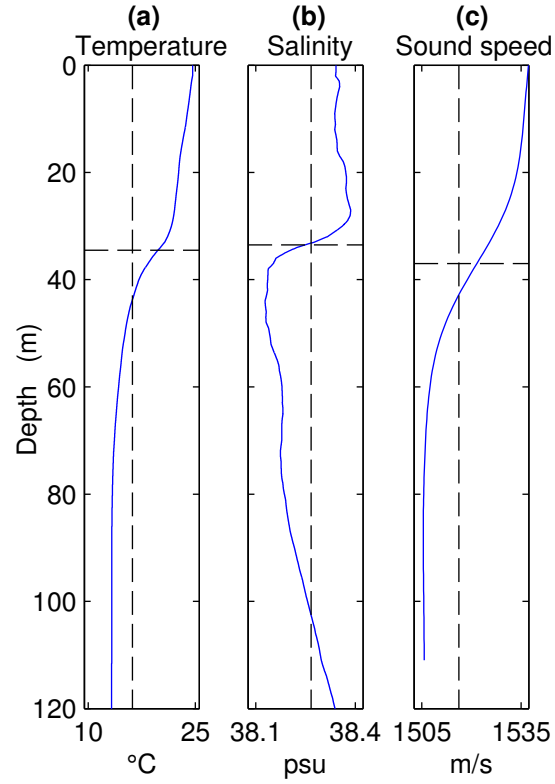


Figure 3.2: FAF05 profiles for temperature (a), salinity (b) and sound speed (c) showing mean (vertical dashed line) and thermocline (horizontal dashed line). These profiles are the average of several CTD casts, and the resulting sound speed profile has been smoothed prior to use in numerical simulations.

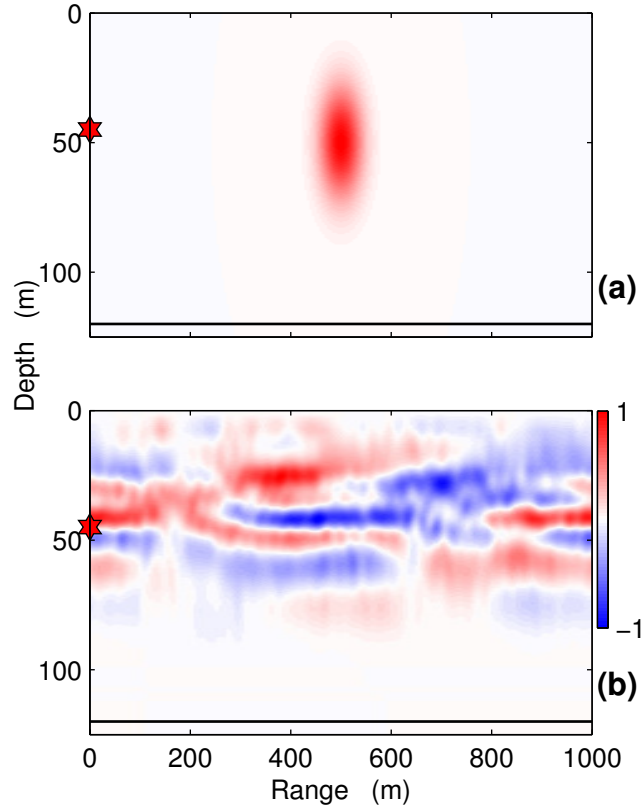


Figure 3.3: Sound-speed perturbations used to probe the performance and linearity of the three sensitivity kernel types. (a): Symmetrical Gaussian sound-speed displacement, with spatial scales of 100m in range and 50m in depth, located in the center of the waveguide. (b): Internal-wave induced sound-speed perturbation for the FAF05 summer profile (Fig. 3.2). Vertical modes are derived from buoyancy parameters measured at sea. Horizontal components are sine and cosine functions. The red star marks the source position (at 45 m depth) used in the numerical simulations presented. The color scale indicates the sound-speed shift in m/s.

readers benefit, but requires a detailed description before proceeding. Each figure is associated with a single peak identified from Fig. 3.1 . The upper, wide panels show the three sensitivity kernels for this peak-arrival (amplitude, phase, and time) with source and receiver positions superposed as red stars and blue circles, respectively. The sensitivity maps are shown in intensities of red and blue color - red indicates that an increase in sound-speed at that location will result in a positive change in the observed quantity (e.g. amplitude), while blue indicates a negative relationship. Eigen-ray paths for this geometry are overlaid as grey lines and the particular rays matched in time with this peak are emphasized in black. The lower subplots aggregate the linearity test results for this peak in a table of plots. The left column shows the amplitude variations as a function of increasing perturbation magnitude; the middle column is phase, and the third column is travel-time (relative to the unperturbed peak value). The first row shows the results using a flat sound-speed change; the second row is for the Gaussian perturbation (Fig. 3.3a); and the third row is for the randomly generated internal-wave sound-speed displacement map (Fig. 3.3b). The perturbed simulation values are plotted with “o” markers, and the kernel estimates added as “x” symbols. For the time and phase plots there is an additional quantity plotted with “+” markers. This represents the secondary estimate calculated from the alternative kernel (Eq. 3.8) - i.e. phase changes determined from the time-kernel and vice versa. The units for amplitude are arbitrary with respect to the numerical model, phase is presented in radians, and time is shown as the change in milliseconds from the unperturbed value.

3.3.2 Linearity figures and discussion

Glancing over all the provided figures, the first feature that stands out as common to all the examples, is that phase and time – observations and estimates – correlate very well for the simple case of the flat sound-speed increase. This lends credence to the assumption that phase and time are directly correlated (via Eq. 3.8), despite the different derivations for their respective sensitivity kernels. For amplitude, common sense would suggest that a uniform sound-speed increase in the environment should have no effect, only accelerating the existing arrival

structure, however we do see a slight change in the amplitude of the observed peaks (perturbed PE) that the amplitude kernel seems unable to predict correctly - however note the small scale on the ordinate for amplitude in most cases. Despite this initial performance concern in the simplest of cases, the amplitude responses for the range-dependent tests (Gaussian, internal-wave) appear mostly linear, and well matched by the kernel estimates.

Figure 3.4 is a peak composed of a single path, reflected off the bottom and subsequently the surface. Both the amplitude and phase kernels show sharp distinct pictures for sensitivity here, while the TSK is more diffuse, with off axis structure that would be unexpected even from a wave-theoretic viewpoint. Despite this odd look, the TSK performs well for all 3 test examples, indicating that this is unlikely to be just an artifact from calculation, and is at least consistent with the PE numerical model from which it was constructed.

Figure 3.5 shows a single path reflected off the bottom. Time and phase diverge for the Gaussian test case, but given the small scales along the vertical axes, and the weak interaction this path would have with that perturbation (the lump would mostly reside above the sensitive areas) the divergence seen may not be that substantial. Even so, this shows that the fine-scale, off-axis structure seen in the TSK is valid as it is the only part of the kernel that should interact with the elevated gaussian perturbation. Note, however, that the observed phase response does not vary at all, as predicted by the phase sensitivity kernel, which would match the ray-centric view of this interaction - that there shouldn't be any change.

Figure 3.7 is similar to Fig. 3.4, in that it exhibits a single ray path with two reflections. As before, we see that the TSK has a more diffuse structure extending off axis than the other two sensitivity kernels. Additionally, there now appear to be patches of sensitivity in the TSK in regions of the environment quite separate from the expected ray path, yet the linearity shown by the TSK for all three test cases is quite good.

Figure 3.7 shows a peak composed of a single high-angle path, the last and weakest arrival seen in this time series. The sensitivity kernels contain some odd

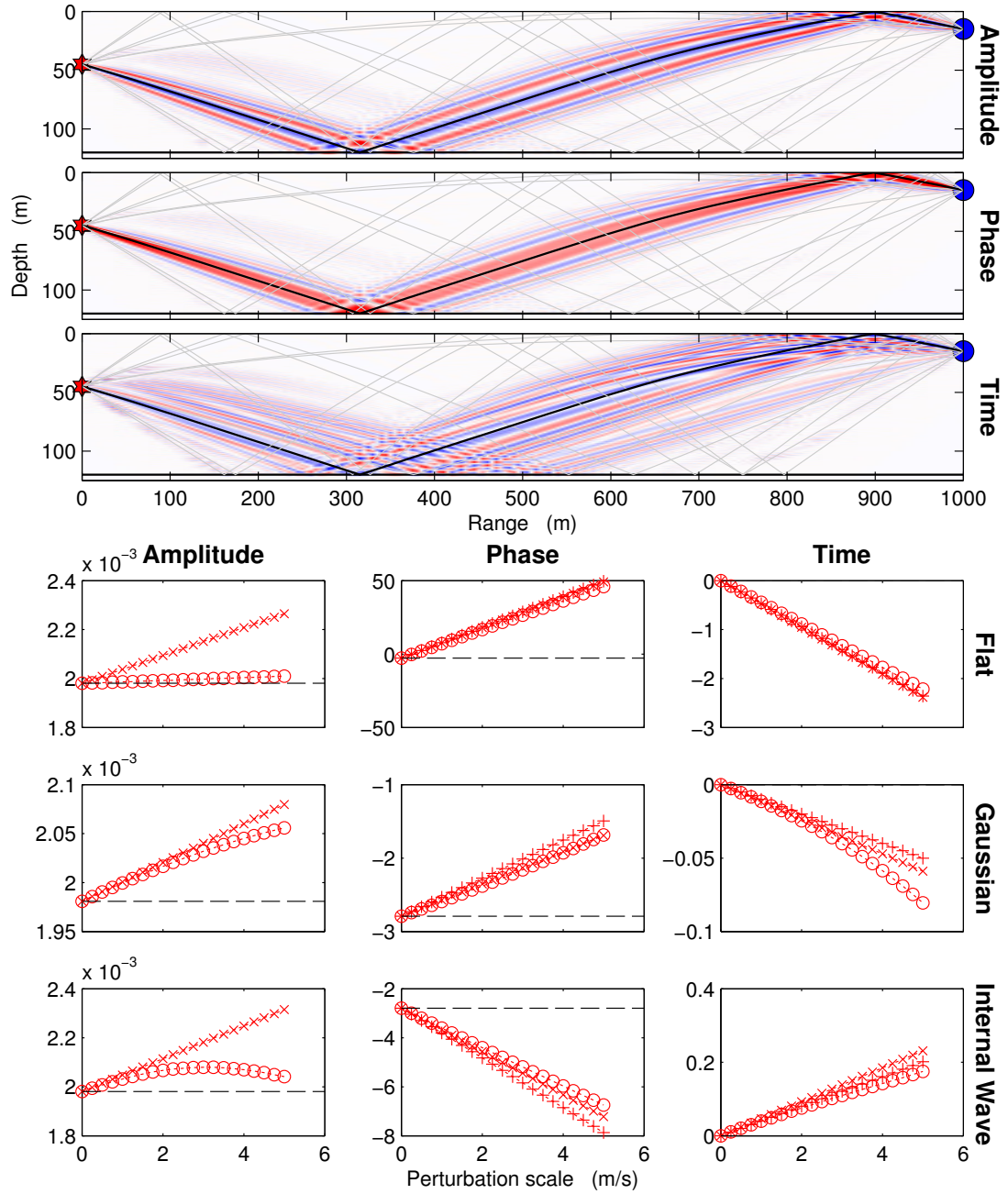


Figure 3.4: For peak #3 (marked red) in the 15 m time series from Fig. 3.1. This arrival time corresponds to a single ray path, with one bottom-reflection and another surface reflection adjacent to the receiver. Please refer to the end of Sec. 3.3.1 for a detailed description of these plots.

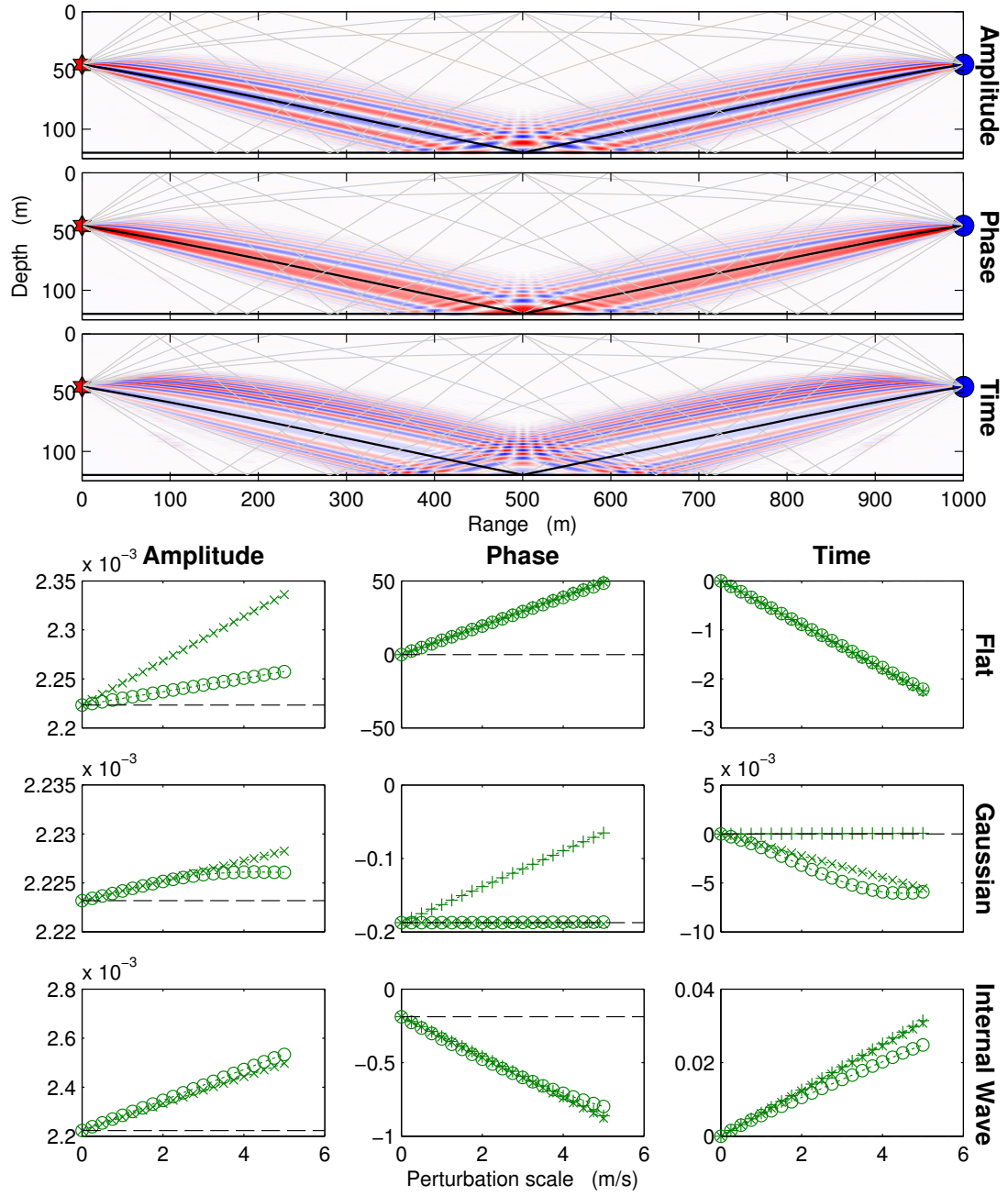


Figure 3.5: For peak #2 (marked green) in the 45 m time series from Fig. 3.1. This arrival time corresponds to a single bottom-reflected symmetric path. Please refer to the end of Sec. 3.3.1 for a detailed description of these plots.

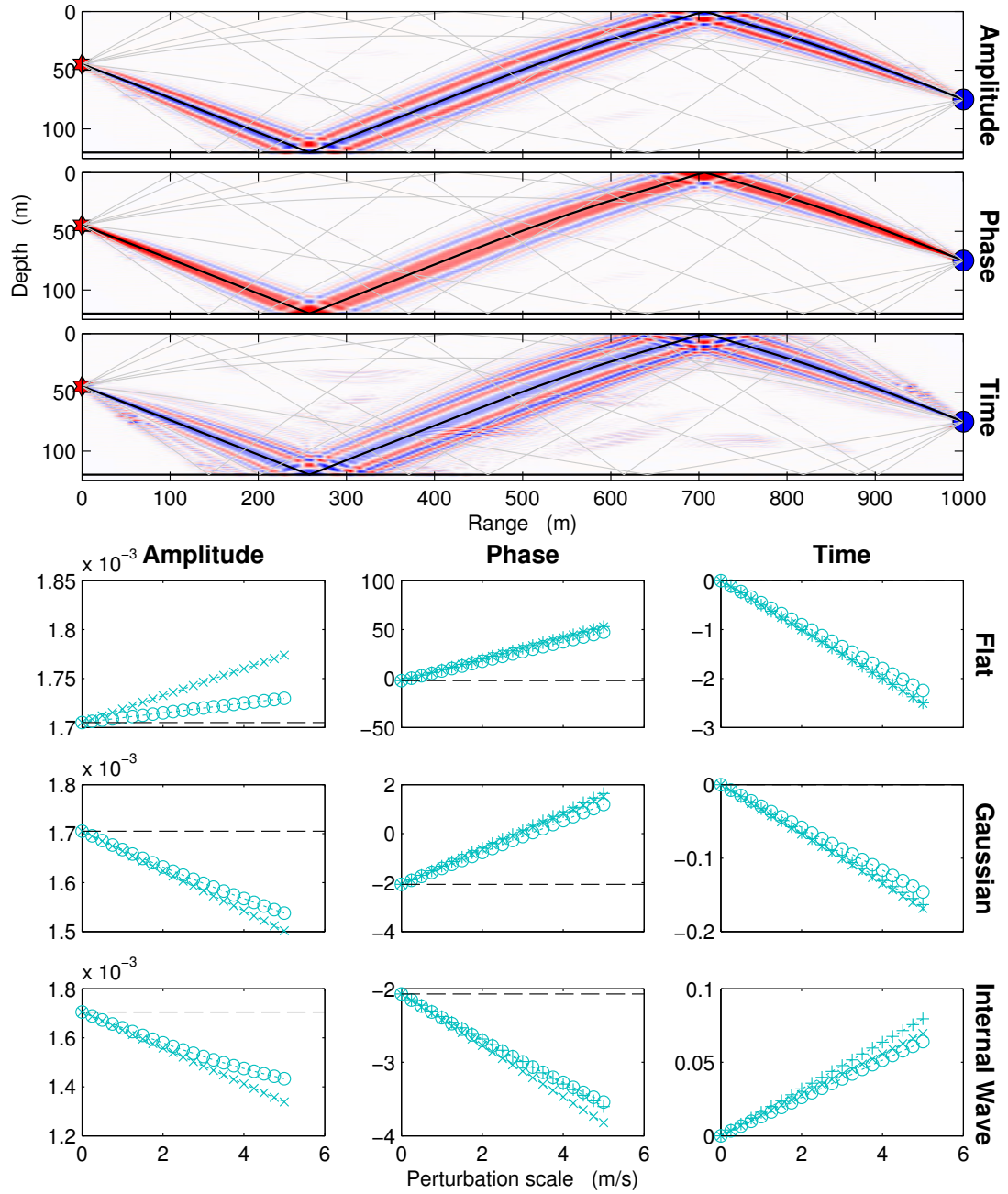


Figure 3.6: For peak #4 (marked teal) in the 75 m time series from Fig. 3.1. This arrival time corresponds to a doubly-reflected single ray path through the environment.

Please refer to the end of Sec. 3.3.1 for a detailed description of these plots.

artifacts, most notably in the TSK, and least prominent in the phase kernel. In fact, the phase kernel does a better job of estimating the time variations than the TSK does in the realistic case, and one has to wonder if these “UFOs” are the culprit.

In all of the above examples, the flat tests show favorable correlation between phase and time and their respective sensitivity kernels, but this is likely because all the high-order structure seen in the TSK averages to zero. In the presence of a more structured sound-speed profile, the phase and travel-time estimates do diverge.

3.3.3 Phase and travel-time sensitivity differences

To further investigate the apparent differences in sensitivity shown between phase and travel-time, a few more linearity tests are presented here. Instead of the arbitrary or internal-wave induced perturbations, the direct subtraction of the phase sensitivity kernel from the (frequency-weighted) travel-time kernel is now used to dictate the spatial shading of the applied sound-speed displacement maps, through which the PE numerical models are run.

If both sensitivity kernels are good estimators of their respective quantities, this difference map should produce a perturbed environment that results in a travel-time change but with no corresponding phase change - which would invalidate the assumption given in Eq. 3.8.

Figure 3.8 shows one such difference map produced for the 2nd peak observed on the receiver at 45 m depth, and one can clearly see that the subtraction has resulted in all sensitivity along the ray-path being removed, leaving just the high-order fringe structure that is only present in the TSK. These maps were produced for all the peaks marked in Fig. 3.1, including the four examples shown above in Sec. 3.3.2, and the same ray/beam masking effect is observed throughout.

These difference maps were used to test the validity of this fine-structure in the TSK for each corresponding peak, scaling the sound-speed displacement from 0 to 2 m/s, in 0.1 m/s increments, and the results for the four examples presented above are summarized in Fig. 3.9. Right away, the plots show that there

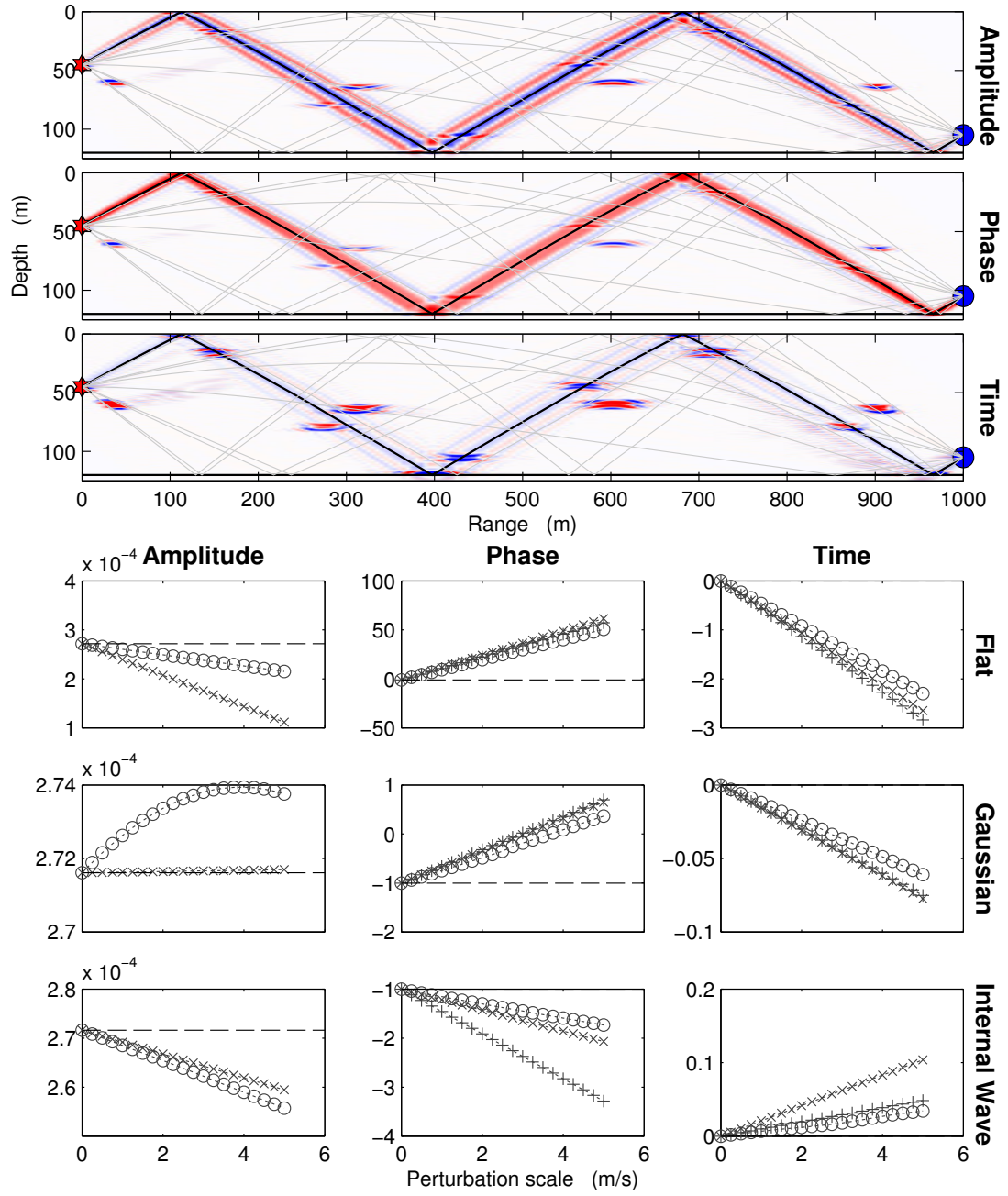


Figure 3.7: For peak #7 (marked black) in the 105 m time series from Fig. 3.1. This arrival time corresponds to the last, and weakest high-angle path. Please refer to the end of Sec. 3.3.1 for a detailed description of these plots.

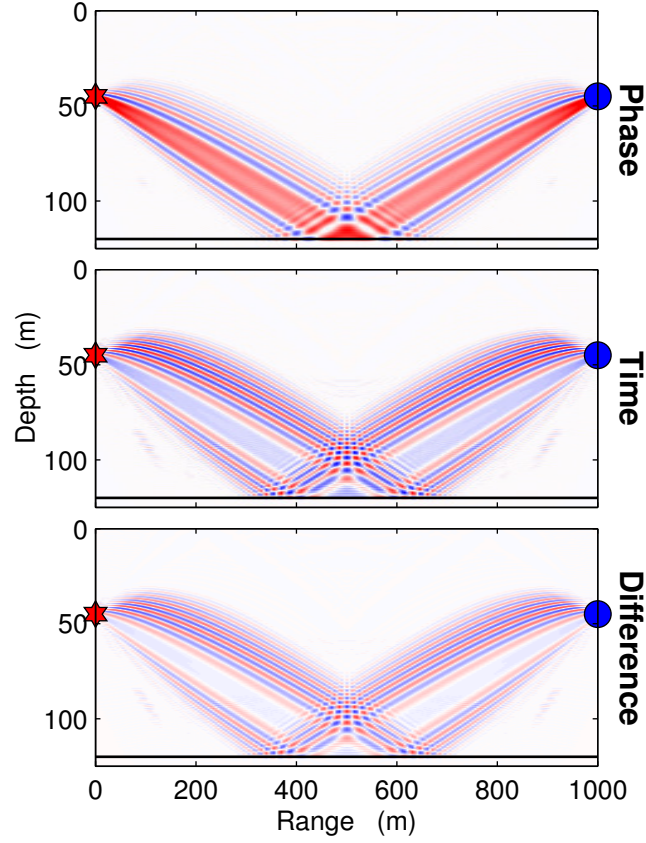


Figure 3.8: Phase and time sensitivity kernel difference map $(w_c \frac{\partial \tau}{\partial c} - \frac{\partial \theta}{\partial c})$, for peak #2 (marked green) in the 45 m time series from Fig. 3.1. Note the loss of sensitivity along the main beam path that results from the subtraction. The linearity test results for this particular peak are provided in Fig. 3.5.

is no substantial change in phase of the observed peaks, which is matched by the phase kernel estimates. Travel-time also does not change substantially, yet the TSK expects there to be a large shift in the temporal position of the peak. Closer inspection of the first few points, around 0.1–0.2 m/s, show's a small change in observed travel-time that does line up with the TSK estimate, but this does not extend any further, as the observed time change levels out - or even returns to the original value in one example.

Most of the induced variability actually occurs in the amplitude of the peak, which is adequately described by the amplitude kernel, until the end of the series when the observed response becomes more non-linear. Figure 3.10 shows the envelope of peak #2 for the 45 m receiver, and how it evolves as the environment is modulated by the difference map given in Fig. 3.8. This clearly shows how the peak remains essentially stationary in time, only changing in amplitude and pulse shape, while the TSK predicts a substantial shift in time.

This discrepancy may be explained by looking back at the derivation of the TSK given by Skarsoulis *et al*[7]. A peak arrival is identified as the top of a pulse, where the gradient of the curve is zero, and defined by

$$\dot{a}(\tau_i; c) = 0,$$

where a is the envelope of the arrival structure, and the overdot represents differentiation with respect to time - as before; and τ_i is the arrival time of the i -th peak with respect to a base sound-speed profile, c . For a sound-speed perturbation, Δc , that induces a time-shift in the peak of $\Delta\tau_i$, the modified peak still satisfies the same requirement,

$$\dot{a}(\tau_i + \Delta\tau_i; c + \Delta c) = 0.$$

At this point, the authors used a first-order Taylor expansion to produce a linear expression for $\Delta\tau_i$,

$$\dot{a}(\tau_i; c + \Delta c) + \ddot{a}(\tau_i; c + \Delta c)\Delta\tau_i = 0. \quad (3.9)$$

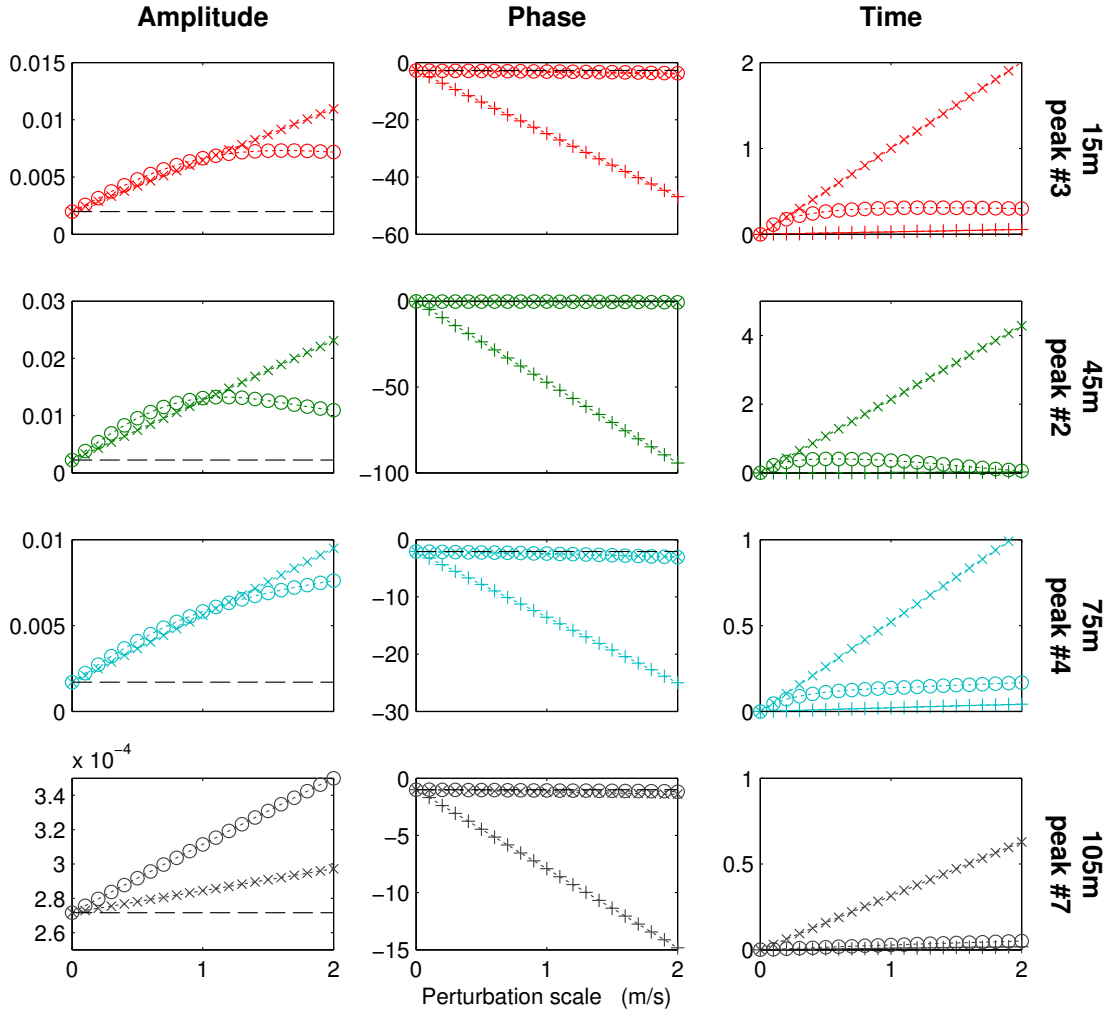


Figure 3.9: Example data tracks from perturbing the numerical models with phase-time sensitivity difference maps (increased up to ± 2 m/s), such as the one shown in Fig. 3.8. PE observations are plotted with “o” markers, primary kernel estimates as “x” symbols, and secondary estimates with “+” markers. Primary estimates are Phase from Phase kernel, Time from Time kernel; secondary estimates are Phase from Time kernel, and Time from Phase kernel. The results are presented as a table of figures, with column labels indicating the data type plotted, while the rows identify the particular peak (from Fig. 3.1) being tracked. Each peak has been perturbed by its own corresponding difference map. Amplitude units are arbitrary with respect to the numerical model, phase is plotted in radians, and time is shown as the change from the unperturbed value in milliseconds.

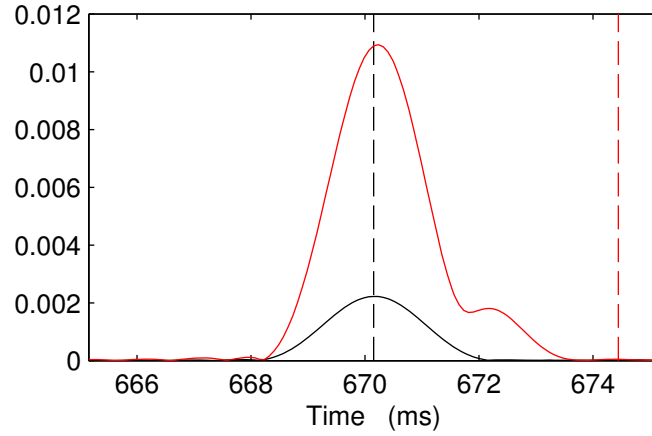


Figure 3.10: Envelope for peak #2 (marked green) in the 45 m time series from Fig. 3.1. The solid black curve represents the unperturbed peak pulse shape, marked in time by the broken black vertical line. The solid red curve shows the pulse shape after the environment has been perturbed by the difference map shown in Fig. 3.8, at a magnitude of 2 m/s. The broken red vertical line marks the shift in time of the peak as expected from the TSK estimate.

Unfortunately, this now implies that the TSK has an explicit dependance on the form of the peak, since the 1st and 2nd time-derivatives of the envelope within Eq. 3.9 are representative of the pulse shape. In contrast, the phase sensitivity kernel given by Eq. 3.6, has no dependance on the peak shape in time, other than what is introduced via the fourier-transform — i.e. it is only a function of bandwidth.

This could explain the extraneous fine-structure present in the TSK, that can be associated with small-scale time shifts in the peak as the amplitude (or shape) changes, but do not represent any actual aggregate change in travel-time. This could also provide reason for the lack of structure seen in the TSK for the weaker late arrivals, such as shown in Fig. 3.7, where the peaks become less defined — intuitively, travel-time sensitivity should have no dependance on peak strength, as long as the signal is discernible above the noise.

3.3.4 Statistics from a time-evolving ocean state

Thus far, the simulation tests indicate that observed acoustic changes to sound-speed perturbations are generally linear in phase and time and well approximated by the sensitivity kernels; and that the phase kernel may even be a better estimator of travel-time changes than the TSK. Amplitude appears to be the most non-linear of the three quantities, and the amplitude sensitivity kernel the lowest performing of the set as well. But these are still just observations from the few examples presented above, so a more thorough statistical investigation is required.

To this end, the internal-wave based test case (Fig. 3.3b) from the summer profile is expanded to encompass all four sources and receivers, and is augmented with more ocean-state instances, in order to simulate data as would be expected from the continuous acoustic monitoring of a time-evolving ocean environment. The spatial modes used to construct these instances are derived from the experimental CTD observations, as before. The spectral weighting of these components is determined randomly, to produce 20 different independent ocean states. These weights are then interpolated over 200 time-steps and initialized at zero for time step #1, to provide a smooth transition from one state to the next, which helps ease peak/data tracking. So the 20 independent ocean states in fact consist of the base unperturbed ocean initially, plus 19 additional random instances.

As before, perturbed PE simulations are computed to produce the 'observed' changes, while simultaneously using the sensitivity kernels to estimate the expected change. This system produces a time series for each observed quantity, plotting both observed and estimated values as a function of ocean state 'time' step. Figure 3.11 shows a few examples of the time series produced for some of the specific peaks already presented earlier. The window plotted is reduced from the full 200-point series in order to show some of the variability more clearly.

These extended tests can now be used to directly quantify the performance of the sensitivity kernels as estimators of acoustic response to sound-speed changes. The value calculated from each time-series set is the Fraction of Variance Explained (FVE), also known as the coefficient of determination, which is given by

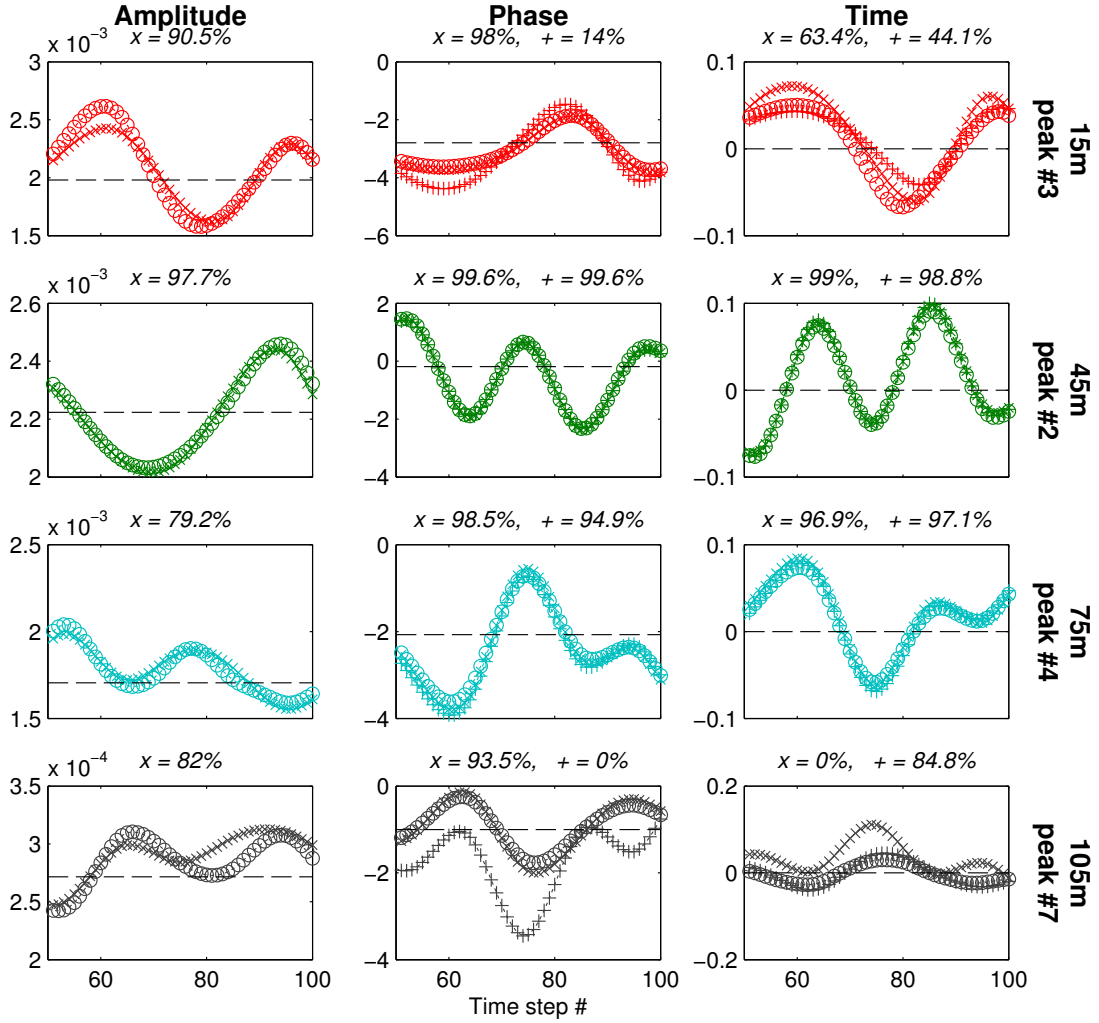


Figure 3.11: Example data tracks from the time-evolving ocean-state tests (with perturbation magnitude ± 3 m/s) presented as a table of figures, with a layout identical to Fig. 3.9. There are 200 total time steps over 20 independent random ocean states, but just 50 points towards the center of the series are presented here as an example to show the variability. The subplot titles show the Fraction of Variance Explained (FVE), or Coefficient of Determination, as a percentage, for the associated estimate - which is a measure of kernel performance. Amplitude units are arbitrary with respect to the numerical model, phase is plotted in radians, and time is shown as the change from the unperturbed value in milliseconds.

$$FVE = 1 - \frac{\sum [y(t) - f(t)]^2}{\sum [y(t) - y_0]^2}, \quad (3.10)$$

where $y(t)$ are the observations (from perturbed PE runs), $f(t)$ are the estimations (from the kernels), and y_0 is a reference or mean value — the base unperturbed quantity is used here. The FVE numbers for the time series shown in Fig. 3.11 are provided in the subplot titles as percentages. The time and phase plots include two values: one for the primary estimate (e.g. phase from phase kernel) and the other for the secondary estimate (e.g. phase from time kernel).

Repeating this process for increasing sound-speed values, as before, the FVE statistics can be aggregated to plot performance as a function of perturbation magnitude, and also filtered to exclude peaks that are known to be problematic (e.g. multipath and/or weak peaks). Figure 3.12 presents a series of histograms that summarizes the performance of each sensitivity kernel under different conditions. Here the performance requirement has been set at $FVE > 0.9$, meaning each bar represents the percentage of data for which the sensitivity kernel can account for at least 90% of the observed variability.

As you can see, the amplitude sensitivity kernel performs the worst out of the three: it's ability to estimate the changes in peak amplitude dropping substantially with increasing perturbation magnitude — similar graphs with lower performance requirements (not shown) indicate that the amplitude kernel can account for only 60–70% of the observed variability in most peaks. Phase, on the other hand, continues to surprise: it consistently outperforms travel-time as a linear observable, and the phase kernel beats the travel-time kernel at it's own game as well. As observed earlier, the latter weaker arrivals are problematic for the TSK, and excluding both weak and multipath peaks evens the charts a little, but these two filtering steps result in the exclusion of $\sim 30\%$ of the peaks each, while the histograms indicate that phase is perfectly functional keeping the weak (amplitude) arrivals.

Putting the sensitivity kernels aside for a moment — the covariance of phase with time can be directly investigated by treating the observed phase as a linear estimator of observed travel-time, and performing the same statistical analysis. The

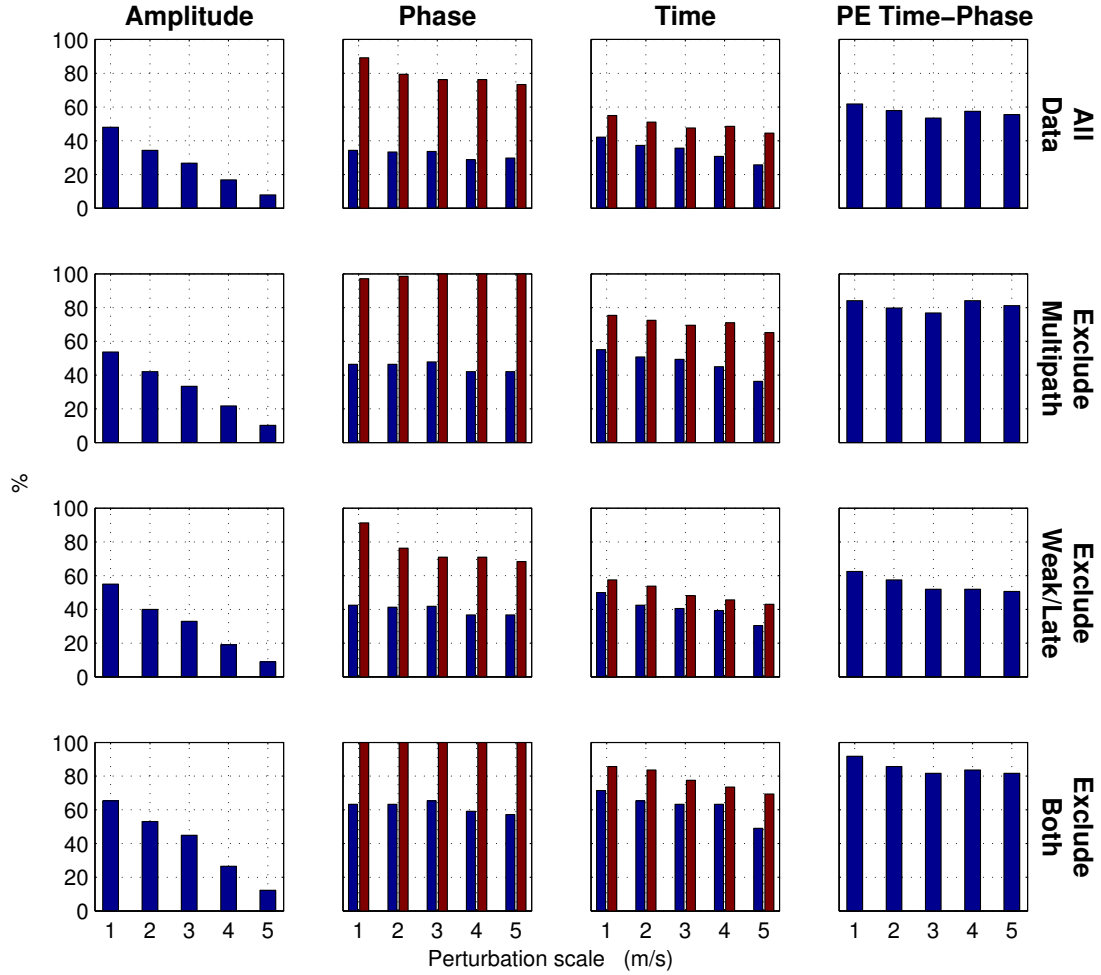


Figure 3.12: Summary statistics for the time-evolving ocean-state tests. The histograms show percentage of data for which each estimator can predict most of the observed variability ($FVE > 0.9$), plotted against increasing perturbation magnitude. In the phase and time diagrams, the blue bars represent the time kernel performance; the red bars are for the phase kernel metrics. Each row shows the same statistics recalculated with different data filtering choices. Excluding multipath keeps only those peaks associated with a single eigenray. Excluding weak peaks retains only the 1st five significant arrivals, throwing out later high-angle peaks. The last column of plots, labeled “PE Time-Phase” show how well observed variations in (peak) travel-time can be explained by observed phase changes.

last column in Fig. 3.12 shows these results for an $FVE > 0.9$, which demonstrates that phase and time only get along 80% of the time at best. This set of histograms also bares a close resemblance to the red bars shown for the phase sensitivity kernel in the time column, indicating that when the phase kernel fails to account for some time variability, it may be because observed phase and travel-time don't track each other any how.

3.4 Discussion and Conclusions

Sensitivity analysis has previously been used to derive a linear relationship between travel-time measurements and sound-speed fluctuations, resulting in the Travel-time Sensitivity Kernel (TSK). Recent work has complimented this by deriving the first Born approximations for amplitude and phase of a complex demodulated signal as well. It was shown that amplitude carried additional information about the medium over phase measurements alone, but it was assumed that phase could be directly related to travel-time and hence added no further detail itself.

Inspection of the two sensitivity kernel equations for phase and time reveals no obvious relationship connecting them, and even their visual structure can appear quite different when calculated for broadband signals. Yet, preliminary tests showed that they produce almost exactly the same quantitative result when considering uniform increases in sound-speed across the environment. More exhaustive linearity tests showed that phase and time estimates do not necessarily correspond to one another in the presence of range-dependent ocean sound-speed structure, and this was frequently matched by perturbed numerical models - phase and time can and do diverge. Investigating the structural differences between the two kernels directly, showed that the fine-scale features present in the TSK are not actually representative of travel-time sensitivity, but rather result in amplitude changes alone with no substantial change in associated phase either. This discrepancy may be traced back to the derivation of the TSK, and it's dependance on peak pulse-shape. Further tests through a simulated time-evolving ocean pro-

vided a statistical analysis of sensitivity kernel performance, that shows phase is a more linear observable than peak travel-time, with respect to monitoring in a short-range varying ocean - and that even considering travel-time measurements alone, the phase sensitivity kernel is a better performing estimator.

As part of this investigation, it was also observed that the amplitude sensitivity kernel was a poor linear estimator in general. While the potential to provide additional information about the environment exists, and amplitude estimates were seen to be quite linear in a few specific cases, its poor linear range on average may limit its use in practical applications.

While the emergence of phase as a good candidate for linear acoustic observations has been suggested by this paper, a few caveats should be noted: firstly, the environment described here was very short range (1 km), and further work needs to be done to see if this phase-time relationship extends to longer ranges and deeper ocean profiles; also, the issue of wrap and circular ambiguity in phase observations requires continuous and frequent measurements to avoid - especially since the work presented here suggests that the use of peak arrival-time to estimate phase, and vice versa, may not always be valid.

Acknowledgements

The text of this chapter is a manuscript in preparation for submission to *The Journal of the Acoustical Society of America*: Jit Sarkar, Bruce D. Cornuelle, and William A. Kuperman, “The phase sensitivity kernel and its performance as a linear travel-time estimator”. The dissertation author was the primary investigator and author of this paper.

References

- [1] Walter H Munk and Carl Wunsch. Ocean acoustic tomography: a scheme for large scale monitoring. *Deep-Sea Res.*, 26(1):23–1, 1979.
- [2] Walter H. Munk, Peter F. Worcester, and Carl Wunsch. *Ocean acoustic to-*

- mography*, chapter 5. Cambridge University Press, Cambridge; New York, 1995.
- [3] Walter H Munk and Carl Wunsch. Ocean acoustic tomography: Rays and modes. *Rev. Geophys. Space Phys.*, 21(4):777–793, Jan 1983.
 - [4] E C Shang. Ocean acoustic tomography based on adiabatic mode theory. *J. Acoust. Soc. Am.*, 85(4):1531–1537, 1989.
 - [5] Gerassimos A Athanassoulis and Emmanuel K Skarsoulis. Arrival-time perturbations of broadband tomographic signals due to sound-speed disturbances. a wave-theoretic approach. *J. Acoust. Soc. Am.*, 97(6):3575–3588, 1995.
 - [6] Emmanuel K Skarsoulis, Gerassimos A Athanassoulis, and Uwe Send. Ocean acoustic tomography based on peak arrivals. *J. Acoust. Soc. Am.*, 100(2):797–813, 1996.
 - [7] Emmanuel K Skarsoulis and Bruce D Cornuelle. Travel-time sensitivity kernels in ocean acoustic tomography. *J. Acoust. Soc. Am.*, 116(1):227–238, 2004.
 - [8] F A Dahlen, S H Hung, and Guust Nolet. Fréchet kernels for finite-frequency traveltimes-I. theory. *Geophys. J. Int.*, 141(1):157–174, 2000.
 - [9] Jeroen Tromp, Carl Tape, and Qinya Liu. Seismic tomography, adjoint methods, time reversal and banana-doughnut kernels. *Geophys. J. Int.*, 160(1):195–216, Jan 2005.
 - [10] Max Born. The quantum mechanics of the impact process. *Z. Phys*, 37(12):863–867, Jan 1926.

Chapter 4

Sensitivity kernel for surface scattering in a waveguide

Abstract

Using the Born approximation, a linearized sensitivity kernel is derived to describe the relationship between a local change at the boundary of an arbitrary wave propagation environment. The structure of the surface scattering kernel is investigated numerically and experimentally for the case of a waveguide at ultrasonic scale. To better demonstrate the sensitivity of the multipath propagation to the introduction of a localized perturbation to the air-water interface, the kernel is formulated both in terms of point-to-point and beam-to-beam representations. Agreement between theory and experiment suggests the potential for application of sensitivity analysis to inversion of sea surface structure.

4.1 Introduction

Surface scattering in a waveguide involves the combination of waveguide propagation and scattering physics[1, 2, 3], both subjects that have been extensively studied separately. From theory and simulation, a series of studies in the late 1980's provided useful descriptors of sea-surface scattering using Kirchhoff

and perturbation approximations[4, 5, 6]. However, most of the above-mentioned analyses are either frequency-domain methods performed with continuous waves or time-domain statistical approaches with only one bounce on the ocean surface (e.g. Dahl[7] and Yang[8]). Other earlier work dealt with the deterministic scattering of a local change at an interface[9].

The main focus of this paper is the isolation of the waveguide effect from the deterministic local surface scattering effect in experimental data in which they are typically merged. Sensitivity kernel analysis[10, 11] provides a methodology to perform this task. In the framework of the single-scattering Born approximation, the sensitivity kernel then could be used for subsequent inversion of the surface structure. The goal of this paper is limited to show with theory and laboratory data that the sensitivity kernel analysis as applied to the waveguide/surface scattering problem indeed separates the waveguide physics of the waveguide from the scattering physics at the air-water interface.

The sensitivity kernel is an expression that relates a change in the acoustic field between a source and a receiver, to a local change in the medium property. Aside from its straightforward use in the forward problem, the sensitivity kernel can be used to invert for environmental change. For example, in underwater acoustics, travel-time tomography has been recently developed with the sensitivity kernel[10] to predict the arrival-time change of the acoustic echoes. Similarly, a recent paper has experimentally shown that the sensitivity kernel for a local change in density[12] could be used for the localization of a target in an ultrasonic waveguide. Both results apply to multipath propagation media (shallow or deep water ocean) in which the acoustic field is perturbed by a local volume change.

In this paper, the sensitivity kernel formulation is examined, both theoretically and experimentally, for a local change at the surface of an acoustic waveguide. In particular, a sensitivity kernel in the Born approximation is derived that determines the change in the acoustic field as a function of a local perturbation in the shape of the surface of the waveguide. The derived results are verified by a laboratory experiment at the ultrasonic scale in which the sensitivity kernel is directly measured by taking the difference between pressure measurements made with and

without the surface perturbation. It is then shown that the sensitivity kernel analysis can be applied to a source/receiver beamformer processing method[13] which isolates the individual eigenrays in the multipath waveguide propagation. The added value of this Double-BeamForming (DBF) process is to separate the effect of the local surface change on each eigenray amplitude and phase, providing then signal to noise ratio and resolution advantages for any subsequent inversion.

In the next section the point-to-point Surface Sensitivity Kernel (SSK) for a local boundary change is derived and the theory then applied to DBF processing between two source-receiver arrays. Experimental results are then presented in an ultrasonic waveguide in section 4.3 and successfully compared with the simulation indicating the potential efficacy of this procedure.

4.2 The Surface Sensitivity Kernel (SSK)

The propagation from a source at \mathbf{r}_s to a field point at \mathbf{r}_r for the unperturbed waveguide is given by the Green's function $G_0(\mathbf{r}_r, \mathbf{r}_s; \omega)$ at frequency ω . When a local perturbation is generated at the air-water interface, the perturbed Green's function is changed into $G(\mathbf{r}_r, \mathbf{r}_s; \omega)$. Manipulating these two Green's functions between two points in \mathbf{r}_s and \mathbf{r}_r , for a set of volume sources, \mathbf{r}' in V , gives:

$$\begin{aligned} G(\mathbf{r}_r, \mathbf{r}_s; \omega) &= G_0(\mathbf{r}_s, \mathbf{r}_r; \omega) \\ &+ \int G(\mathbf{r}_r, \mathbf{r}'; \omega) \nabla^2 G_0(\mathbf{r}_s, \mathbf{r}'; \omega) \\ &- G_0(\mathbf{r}_s, \mathbf{r}'; \omega) \nabla^2 G(\mathbf{r}_r, \mathbf{r}'; \omega) dV. \end{aligned} \quad (4.1)$$

Applying Green's identity,

$$\int_V g \nabla \cdot \mathbf{f} dV = - \int_V (\nabla g) \cdot \mathbf{f} dV + \oint_S g \mathbf{f} \cdot \mathbf{n} dS, \quad (4.2)$$

and the reciprocity of the Green's functions, produces

$$G(\mathbf{r}_r, \mathbf{r}_s; \omega) = G_0(\mathbf{r}_r, \mathbf{r}_s; \omega) + \oint G(\mathbf{r}_r, \mathbf{r}'; \omega) \nabla_n G_0(\mathbf{r}_s, \mathbf{r}'; \omega) dS \quad (4.3)$$

where the integration is performed over the unperturbed surface so what would have been the second surface integral vanishes since G_0 vanishes on the flat surface. ∇_n is defined as the gradient operator multiplied by an unitary vector perpendicular to the unperturbed interface. G can then be expanded around the unperturbed surface using Δh as the perturbed surface,

$$G(\mathbf{r}_r, \mathbf{r}'; \omega) + \Delta h \nabla_n G_0(\mathbf{r}_r, \mathbf{r}'; \omega) = 0 \quad (4.4)$$

so that Eq. 4.3 becomes

$$G(\mathbf{r}_r, \mathbf{r}_s; \omega) = G_0(\mathbf{r}_r, \mathbf{r}_s; \omega) - \oint \nabla_n G_0(\mathbf{r}_r, \mathbf{r}'; \omega) \Delta h(\mathbf{r}') \nabla_n G_0(\mathbf{r}_s, \mathbf{r}'; \omega) dS \quad (4.5)$$

where only the first term in the Δh expansion is kept. Now, Δh represents a surface whose height is being evaluated at the horizontal surface *point* corresponding to the position vector, \mathbf{r}' (with depth component, $z = 0$).

Therefore, the SSK for a source-receiver pair in $(\mathbf{r}_s, \mathbf{r}_r)$ is given by

$$\begin{aligned} K(\mathbf{r}_r, \mathbf{r}_s, \mathbf{r}'; \omega) &= \frac{G(\mathbf{r}_r, \mathbf{r}_s; \omega) - G_0(\mathbf{r}_r, \mathbf{r}_s; \omega)}{\Delta h(\mathbf{r}')} \\ &= -\nabla_n G_0(\mathbf{r}_r, \mathbf{r}'; \omega) \nabla_n G_0(\mathbf{r}', \mathbf{r}_s; \omega) \end{aligned} \quad (4.6)$$

where it should be noted that the normal derivatives are taken with respect to the unperturbed surface at the position \mathbf{r}' . For a source with spectrum $P_s(\omega)$, the change in the pressure field due to the local perturbation Δh on an elementary surface dS is then,

$$\begin{aligned} \Delta p(\mathbf{r}_r, \mathbf{r}_s, \mathbf{r}'; t) &= \\ &= -\frac{1}{2\pi} \iint \nabla_n G_0(\mathbf{r}_r, \mathbf{r}'; \omega) \nabla_n G_0(\mathbf{r}', \mathbf{r}_s; \omega) \\ &\quad \Delta h(\mathbf{r}') P_s(\omega) e^{-i\omega t} d\omega dS. \end{aligned} \quad (4.7)$$

Here, the important point to note is that Eqs. 4.6 and 4.7 will be used as the basis for the experimental demonstration discussed in section 4.3. That is, the sensitivity kernel multiplied by the surface perturbation can be measured, by taking the difference between the arrivals for the flat and perturbed surface

waveguide propagation. By showing experimental agreement with the theory, it is demonstrated that unperturbed propagation can be used to calculate the sensitivity kernel.

Double beamforming (DBF) transformation

In an acoustic waveguide, the expression of $G_0(\mathbf{r}_r, \mathbf{r}_s; \omega)$ is made complicated by the multipath propagation. Taking advantage of the source and receiver arrays on each side of the waveguide, it appears useful to beamform the acoustic field on both ends through the Double Beamforming (DBF) process. DBF consists of projecting the Green's function over the eigenrays of the waveguide through their launch and arrival angles (θ_s, θ_r) as:

$$G_0^{\text{DBF}}(\theta_r, \theta_s; \omega) = \frac{1}{N_s} \frac{1}{N_r} \sum_S \sum_R G_0(\mathbf{r}_r, \mathbf{r}_s; \omega) \exp[-i\omega(\tau(\theta_s, z_s) + \tau(\theta_r, z_r))] \quad (4.8)$$

with:

$$\tau(\theta_s, z_s) = \frac{(z_s - z_0) \sin \theta_s}{c} \quad (4.9)$$

where z_0 is the center of the N_s -element source array and $\tau(\theta_r, z_r)$ is calculated the same way for the N_r -element receiver array. Note that Eq. 4.9 corresponds to plane-wave beamforming, in the case of a uniform sound speed along the array. With a depth-dependent sound-speed profile the optimal time-delay, $\tau(\theta, z)$, is obtained by the turning-point filter approach[14].

When the data is satisfactorily described by ray approximations, the DBF process extracts from the recorded data matrix the acoustic contribution of every eigenray propagating between the source-receiver arrays, as defined by its launch/arrival angles:

$$p^{\text{DBF}}(\theta_r, \theta_s; t) = \frac{1}{2\pi} \int G_0^{\text{DBF}}(\theta_r, \theta_s; \omega) P_s(\omega) e^{-i\omega t} d\omega \quad (4.10)$$

When the DBF process is applied to each point-to-point signal of the source-receiver arrays, the SSK for a perturbation at \mathbf{r}' is modified in the following way:

$$\begin{aligned}
K^{\text{DBF}}(\theta_r, \theta_s, \mathbf{r}'; \omega) = & -\frac{1}{N_s} \frac{1}{N_r} \sum_S \sum_R \\
& \nabla_n G_0(\mathbf{r}_r, \mathbf{r}'; \omega) \nabla_n G_0(\mathbf{r}', \mathbf{r}_s; \omega) \\
& \exp[-i\omega(\tau(\theta_s, z_s) + \tau(\theta_r, z_r))] \quad (4.11)
\end{aligned}$$

which can be rewritten as:

$$\begin{aligned}
K^{\text{DBF}}(\theta_r, \theta_s, \mathbf{r}'; \omega) = & \\
& -\nabla_n \left(\frac{1}{N_s} \sum_S G_0(\mathbf{r}', \mathbf{r}_s; \omega) \exp[-i\omega\tau(\theta_s, z_s)] \right) \\
& \nabla_n \left(\frac{1}{N_r} \sum_R G_0(\mathbf{r}_r, \mathbf{r}'; \omega) \exp[-i\omega\tau(\theta_r, z_r)] \right) \quad (4.12)
\end{aligned}$$

The first gradient applies to the eigenray issued from the center of the source array and measured at the surface perturbation at \mathbf{r}' , while the second one applies to the eigenray that connects \mathbf{r}' to the center of the receiver array.

For a given eigenray, the beamformed Green's functions

$$G_0^{\text{BF}}(\mathbf{r}', \theta_s; \omega) = \frac{1}{N_s} \sum_S G_0(\mathbf{r}', \mathbf{r}_s; \omega) \exp[-i\omega\tau(\theta_s, z_s)]$$

and

$$G_0^{\text{BF}}(\mathbf{r}', \theta_r; \omega) = \frac{1}{N_r} \sum_R G_0(\mathbf{r}_r, \mathbf{r}'; \omega) \exp[-i\omega\tau(\theta_r, z_r)]$$

locally behave as plane waves in the acoustic waveguide, which leads to the following approximation for the gradient calculation:

$$K^{\text{DBF}}(\theta_r, \theta_s, \mathbf{r}'; \omega) = G_0^{\text{BF}}(\mathbf{r}', \theta_s; \omega) G_0^{\text{BF}}(\mathbf{r}', \theta_r; \omega) \frac{\omega^2}{c^2} \sin\tilde{\theta}_s \sin\tilde{\theta}_r \quad (4.13)$$

where $\tilde{\theta}_s$ (resp. $\tilde{\theta}_r$) corresponds to the eigenray angle between the source array center and \mathbf{r}' (resp. the receiver array center and \mathbf{r}'). Note that $\theta_s = \tilde{\theta}_s$ and $\theta_r = \tilde{\theta}_r$ when \mathbf{r}' is located on the eigenray(θ_s, θ_r) at the air-water interface. Finally,

the change in the DBF pressure field due to the local perturbation Δh over an elementary surface dS is then:

$$\begin{aligned} \Delta p^{\text{DBF}}(\theta_r, \theta_s, \mathbf{r}'; t) = \\ \frac{1}{2\pi} \iint G_0^{\text{BF}}(\mathbf{r}', \theta_s; \omega) G_0^{\text{BF}}(\mathbf{r}', \theta_r; \omega) \frac{\omega^2}{c^2} \\ \sin \tilde{\theta}_s \sin \tilde{\theta}_r \Delta h(\mathbf{r}') P_s(\omega) e^{-i\omega t} d\omega dS \end{aligned} \quad (4.14)$$

From Eqs. 4.14 and 4.13, one derives the expression for both the amplitude and travel-time SSK of each eigenray path. As shown by Marandet *et al.*[12], the DBF-SSK for the normalized amplitude is numerically computed for any \mathbf{r}' between the source and the receiver arrays as:

$$\Delta A^{\text{DBF}}(\theta_r, \theta_s, \mathbf{r}') = \frac{\Delta p^{\text{DBF}}(\theta_r, \theta_s, \mathbf{r}'; \tau)}{p^{\text{DBF}}(\theta_r, \theta_s; \tau)} \quad (4.15)$$

for a given eigenray defined by its launch/arrival angles θ_s, θ_r and travel time τ .

Similarly, the DBF-SSK for travel time[13] is obtained by:

$$\begin{aligned} \Delta \tau^{\text{DBF}}(\theta_r, \theta_s, \mathbf{r}') = \\ \frac{1}{\pi \ddot{p}^{\text{DBF}}(\theta_r, \theta_s, \tau)} \iint i\omega G_0^{\text{BF}}(\mathbf{r}', \theta_s; \omega) G_0^{\text{BF}}(\mathbf{r}', \theta_r; \omega) \frac{\omega^2}{c^2} \\ \sin \tilde{\theta}_s \sin \tilde{\theta}_r \Delta h(\mathbf{r}') P_s(\omega) e^{-i\omega \tau} d\omega dS \end{aligned} \quad (4.16)$$

where $\ddot{p}^{\text{DBF}}(\theta_r, \theta_s, \tau)$ is the second-order time derivative of the DBF field at the eigenray arrival time τ .

4.3 Experimental measurement of surface sensitivity

An ultrasonic laboratory experiment was used to verify the SSK formulation. As imposed by the Born approximation, the sensitivity kernel corresponds to

a small change in the acoustic field with respect to a local change of the environment. In this experimental demonstration, the acoustic field is measured before and after a local surface perturbation, the surface being sequentially perturbed at all ranges between the source and the receiver arrays.

Figure 4.1 illustrates the experimental set-up. Two coplanar ultrasonic arrays, of 64 transducers each, face one another in a 610 mm long, 52 mm deep waveguide. Each transducer has a central frequency of 3.5 MHz (wavelength $\lambda \approx 0.4$ mm), with a 1.5 MHz frequency bandwidth. The size of each element of the linear arrays is 0.75 mm \times 12 mm, which makes the sensor arrays relatively omnidirectional in the plane defined by the source–receiver pair, and also very collimated outside this plane, limiting acoustic echoes from the tank sidewalls. The bottom of the waveguide is made of steel, for which the boundary conditions are nearly perfectly reflecting at the water–bottom interface.

The data acquisition process consists of recording the impulse response between each source and each receiver in the time-domain. A fast way to perform this acquisition is by proceeding through a round-robin sequence, during which each source successively emits a 0.5 μ s broadband pulse at the central frequency of the transducers[15]. The duration between the emitted pulse from each source is chosen to be no longer than the maximum dispersion time in the waveguide (~ 100 μ s), which optimizes the time required to record the full waveguide transfer matrix.

The probe used to perturb the surface is a lead sphere of diameter 5 mm (Fig. 4.1b). It is mounted on a rigid arm suspended above the tank from a remotely-controlled step-motor that allows for fine-scale linear displacements. The probe's initial position is adjacent to the source array. During the course of the experiment the sphere is applied to the surface producing a local perturbation on the order of a millimeter. It is then raised above the waterline before translating horizontally to the next position along the source-array/receiver-array plane, limiting the creation of ripples within the tank.

This is repeated in 1 mm increments across the whole horizontal range between the two arrays, and transmissions are made for the probe in both the up

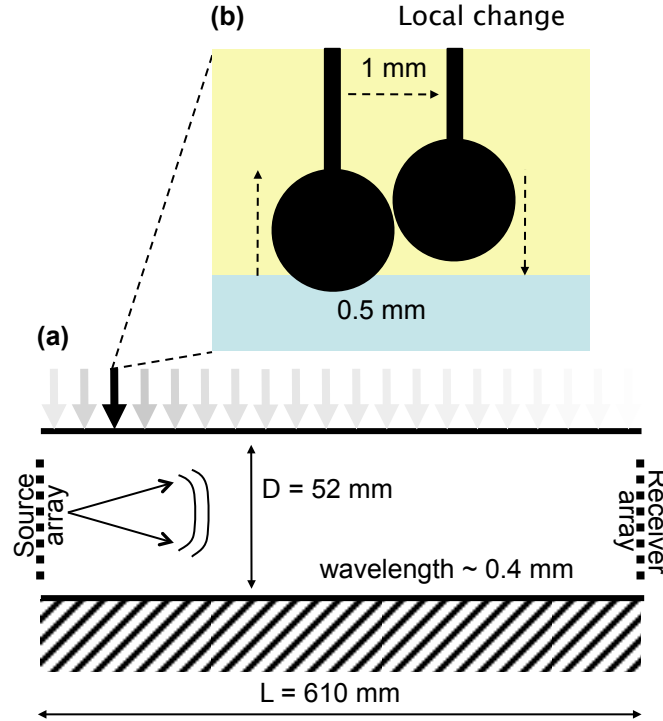


Figure 4.1: Schematic diagram showing the dimensions of the laboratory tank experiment.

(a) - The source/receiver coplanar arrays consist of 64 ultrasonic transducer-elements, each of size $0.75 \text{ mm} \times 12 \text{ mm}$ (*vertical* \times *horizontal*). The source-receiver arrays span the whole water column.

(b) - A 5 mm lead sphere serves as a probe to impact the air-water interface [black arrow in (a)]. The penetration of the sphere inside the waveguide is on the order of one millimeter. Acquisitions between the source-receiver arrays are performed in the time domain for probe positions varying sequentially from the source-array to the receiver-array in 1 mm increments.

and down position at each location. The primary argument for repeating the 'up' probe acquisition at each point in range, as opposed to using a single unperturbed reference field, is to mitigate any other changes that may have occurred in the tank during the course of the experiment. As a matter of fact, it has been observed that the (unperturbed) pressure field for the 'up' probe position slowly varies due to changes within the environment, which is caused by both the warming of the water in the tank and a slight evaporation over the 10-hour duration of the experiment.

4.3.1 Tank data vs. synthetic point-to-point SSK

Figure 4.2a shows an impulse response as recorded on the receiver array due to a transmission from a source element at mid-depth in the water-column. The arrival structure seen is a basic accordion, characteristic of a simple Pekeris waveguide, exhibiting several acoustic wavefronts that have reflected from the boundaries. Figure 4.2b presents the pressure field for one particular receiver element (#32), showing the arrival peaks associated with the multipath propagation. Variations in the echo amplitudes and travel times will be observed as the probe is applied to different ranges r' across the water surface.

The experimental sensitivity, $\Delta p(\mathbf{r}_r, \mathbf{r}_s, \mathbf{r}'; t)$, is calculated for a particular source-receiver pair $(\mathbf{r}_s, \mathbf{r}_r)$ as the pressure field difference between the data for the up and down probe states, and is repeated as a function of the probes position in range, \mathbf{r}' . The difference of these two measurements magnifies the interference effect between the acoustic paths and the scattering on the local surface perturbation, resulting in the sensitivity for intensity shown in Fig. 4.3a.

The residual asymmetry in magnitude seen in the experimentally-observed sensitivity is attributed to a slight evolution of the penetration depth $\Delta h(r')$ of the probe when the probe source scans the waveguide surface from the source array to the receiver array.

A parabolic equation (PE) model is created to simulate propagation through the ultrasonic tank environment, and the results used to produce a numerical sensitivity as defined by Eq. 4.7. The experimental result shows a great deal of congruence with the numerical one (Fig. 4.3b).

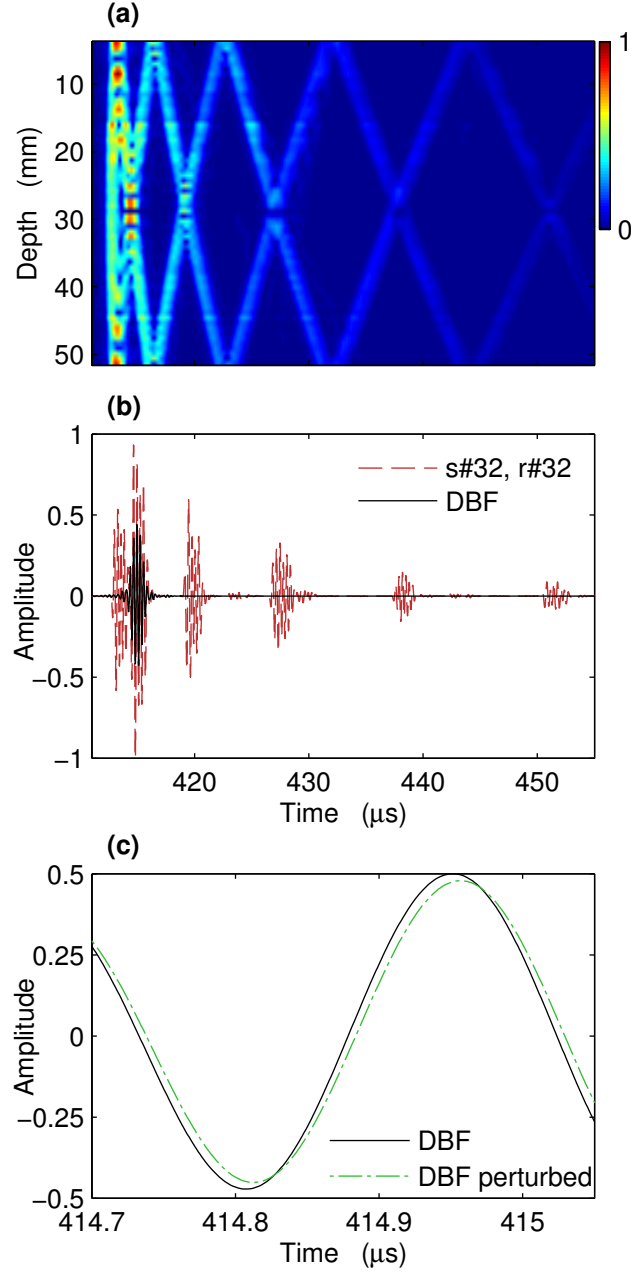


Figure 4.2: (a) - Envelope of the time-domain impulse response across the receiver-array as measured in the tank for a pulse transmission from element #32 on the source-array. Color scale represents normalized pressure. (b) - Normalized pressure-time series as measured on receiver element #32 (broken line), and equivalent double beamformer output from focusing two source-receiver subarrays on the eigenray path (with grazing-angle incidence $\sim 5^\circ$) identified as number 1 in Fig. 4.4 (solid line). (c) - Magnified plot of the peak-time around the single wave-packet produced in the double beamformer output (solid line), with the equivalent view of the perturbed data set (broken line) resulting from the presence of the probe at the surface at range 300 mm. Note the small amplitude and travel-time change (on the order of a few %) associated with this low grazing-angle incident eigenray.

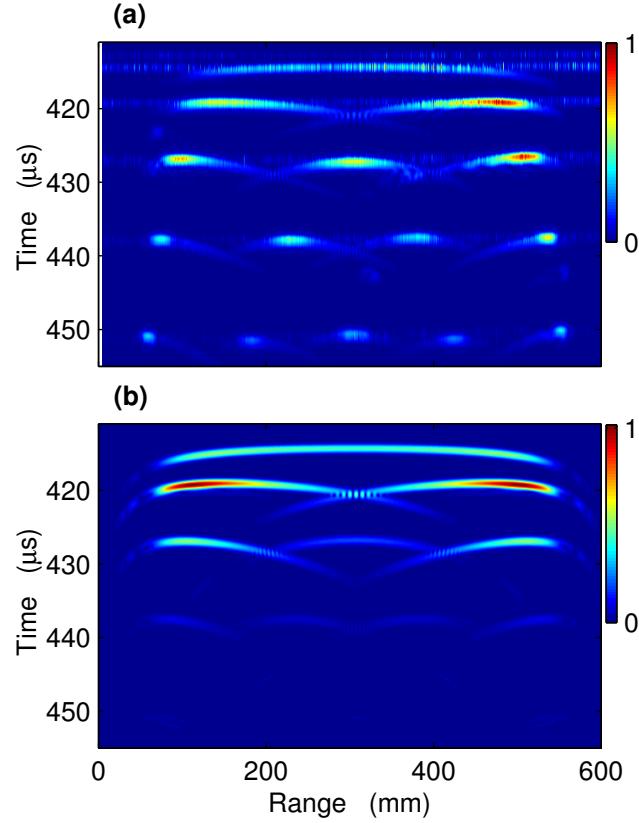


Figure 4.3: (a) - Experimental surface sensitivity (intensity), produced by the difference between 'up' and 'down' field measurements when the probe is raised and lowered, plotted as a function of probe position in range r' . (b) - Theoretical surface sensitivity (intensity) calculated by Eq. 4.7 and convolved with the surface perturbation shape, $\Delta h(r')$, to better approximate the experimentally observed sensitivity. Color scales represent the induced change in measured pressure in arbitrary linear units, normalized to the maximum of each plot.

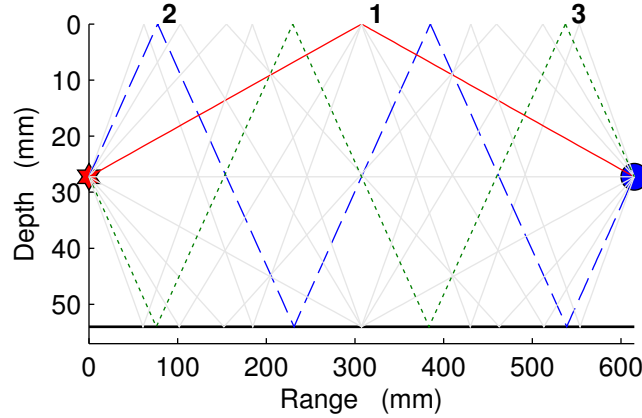


Figure 4.4: Eigenray paths associated with the geometry between source #32 and receiver #32 show which paths interact with the surface, and at what locations. Path #s 1 and 2 correspond to one bounce and two bounces at the water-air interface, respectively. Path #3 is the symmetric equivalent of #2, with two surface bounces as well, but with opposite launch-arrival angles. Though Paths #s 2 and 3 arrive at the same time, their individual contributions may be separated through double beamforming.

For a better physical understanding of the sensitivities shown in Fig. 4.3, the eigenray paths are plotted in the waveguide for this particular source-receiver pair (Fig. 4.4). For each eigenray, the surface sensitivity magnitude is maximal at ranges where the eigenray interacts with the air-water interface. In the case of multiple bounces along the surface, several local maxima in the sensitivity picture are observed. The spatial shape of the surface sensitivity is strongly dependent on the incident angle of the eigenray at the air-water interface, exhibiting a smaller footprint for eigenray paths with higher incident grazing-angles.

4.3.2 Double beamforming treatment

When DBF is applied over two source-receiver subarrays centered on a source-receiver pair, each acoustic echo is isolated according to its launch-arrival beamforming angles. For example, the plain signal in Fig. 4.2b corresponds to a surface bounce that is separated from the bottom bounce after DBF on two source-receiver subarrays when they interfere together for a point-to-point measurement made for a source-receiver pair at the middle of the water column (dashed signal

in Fig. 4.2b). As observed in the example displayed in Fig. 4.2c, the DBF signal for the lowered position of the probe is always delayed in time compared to the no-probe DBF signal, which is surprising since one would intuitively expect the surface perturbation to shorten the travel-time.

Actually, when the small lead sphere touches the air-water interface, three effects are probably in competition. On the one hand, the penetration of the lead sphere in the waveguide creates a depression of the surface that shortens the travel-time. On the other hand, capillary action around the lead sphere locally raises the water level which counterbalances the first effect. Finally, the presence of the lead sphere also changes the local boundary condition at the water-air interface from pressure release which may induce a phase shift on the received signals when the sphere touches the interface. In consequence, the sphere + meniscus footprint at the surface is more complicated than the simple point perturbation assumed by the theory. However, the combination of these effects are limited to a few percent of related amplitude change and travel-time perturbation (Fig. 4.2c). As such, the Born approximation remains valid and so does the calculation of the surface sensitivity kernel. While quantifying the actual sensitivity to the sphere/meniscus perturbation is beyond the scope of this paper, the sphere/meniscus surface perturbation is observed to behave as an “effective” positive local point perturbation of height $\Delta h(r') > 0$.

The experimental DBF-SSK is then calculated as the pressure field difference $\Delta p^{\text{DBF}}(\theta_r, \theta_s, \mathbf{r}'; t)$ measured for the up and down probe position (Fig. 4.5). From the DBF signal in Fig. 4.5, the amplitude and travel-time DBF-SSK can be measured separately as a function of the probe range for each eigenray. The DBF-SSK for the amplitude is calculated as the relative amplitude change of the DBF signals between the up and down probe positions, while the DBF-SSK for travel-time is calculated as the difference between the travel-times of the DBF signals. Figure 4.5 represents the experimental results for both travel-time and amplitude DBF-SSK, for different eigenrays in the waveguide. A good agreement is observed with the theoretical approach derived in the section 4.2 for both $\Delta A^{\text{DBF}}(\theta_r, \theta_s, \mathbf{r}')$ and $\Delta \tau^{\text{DBF}}(\theta_r, \theta_s, \mathbf{r}')$. In the calculation of the theoretical DBF-SSK, a volume

fluctuation $dV = dS \Delta h(r') \sim 80 \text{ mm}^3$ was used to match the experimental DBF-SSK for both travel time and amplitude, as required in Eqs. 4.14 and 4.16. Note that this value of dV is similar for all eigenrays in the waveguide. Though dV should theoretically refer to the volume fluctuation induced by the lead sphere only, it must also practically account for the 12-mm lateral dimension of each array element that was not included, for sake of simplicity, in the sensitivity kernel formulation in both the point-to-point and DBF approaches (Eqs. 4.7 and 4.14). Given the 5-mm diameter of the lead sphere, a heuristic calculation of dS assumes $dS = 12 \times 5 \text{ mm}^2$ to first order, from which $\Delta h(r') \sim 1.3 \text{ mm}$ is obtained, which is a realistic value for the effective surface perturbation in the context of this experiment.

The results for both amplitude and travel-time confirm that the spatial extent of the DBF-SSK is strongly dependent on the grazing-angle of incidence at the air-water interface, which was already observed on the point-to-point sensitivity displayed in Fig. 4.3. Note that the relative amplitude change $\Delta A^{\text{DBF}}(\theta_r, \theta_s, \mathbf{r}')$ varies from 6% to 30% for the same surface perturbation Δh and grazing angles of $\sim 5^\circ$ and $\sim 18^\circ$, respectively. The travel-time perturbation varies in the same proportion from 2% to 10% of the central period. Of course, measurement of such small travel-time fluctuations is polluted by noise even in the case of strong signal-to-noise ratio as observed in Figs. 4.5b and 4.5d. Despite the applications of DBF, a small residual contribution of the symmetric eigenray (Path 3 in Fig. 4.4) is also observed in the experimental sensitivity (time and amplitude) extracted for Path 2 (Figs. 4.5c and 4.5d). Finally, both experimental and theoretical results show the range dependence in r' of the travel-time and amplitude DBF-SSK for the eigenray that bounces twice at the air-water interface. This magnifies the range dependence of the DBF-SSK as expected from the product of the beamformed Green's function $G_0^{\text{BF}}(\mathbf{r}', \theta_s; \omega) G_0^{\text{BF}}(\mathbf{r}', \theta_r; \omega)$ in Eqs. 4.14 and 4.16.

It is important to point out that the above DBF-SSK approach is restricted to a deterministic local perturbation at the interface. Hence the perturbation is of order Δh as opposed to stochastic random interfaces for which the leading perturbation is of order $\langle \Delta h^2 \rangle$. In the literature, many authors dealt with the coherent

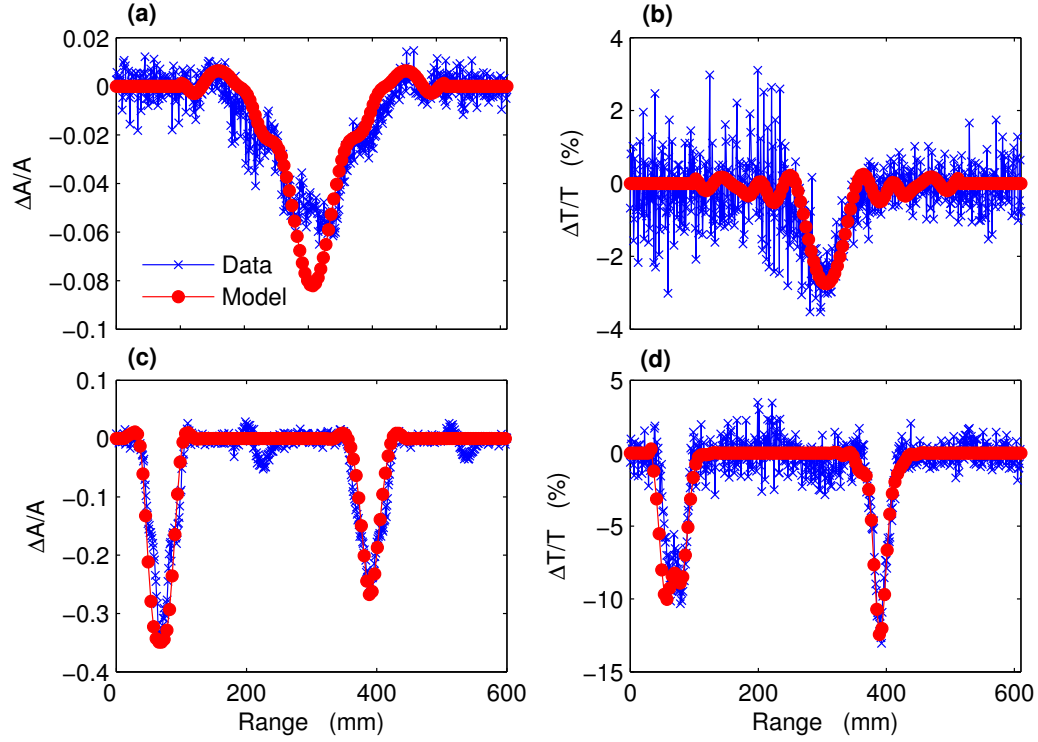


Figure 4.5: Double-beamformed results for both experimental and theoretical sensitivity kernels

Panels (a) & (b) show the amplitude and time kernels, respectively, for a steering angle of $+5.05^\circ$ on both arrays. This represents focus on the peak at time $410 \mu\text{s}$ in Fig 4.3, corresponding to the eigenray path number 1 in Fig. 4.4.

Panels (c) & (d) present the equivalent results for the peaks along time $438 \mu\text{s}$ in Fig 4.3, corresponding to the eigenray path number 2 in Fig. 4.4. The steering angles in this case are $+18.07^\circ$ on the source array and -18.07° on the receive array.

average of an incident plane wave at the rough air-water interface. As detailed by Ogilvy[4], they either formulate this problem in terms of the perturbation theory through an average reflection coefficient for a modified boundary condition or in the frame of the Kirchhoff approximation[5] where the coherent loss is obtained from the phase averaging over realizations of the random surface. Here, none of these approaches apply since the sensitivity kernel approach limits the investigation to a first order deterministic perturbation Δh consistent with the Born approximation.

4.4 Conclusion

An expression that linearly relates perturbations in the air-water interface, to changes in the measured acoustic field has been derived in a waveguide. This Surface Sensitivity Kernel (SSK) provides a picture of how surface structure influences the multi-reflected acoustic propagation between two point elements, source and receiver. The SSK formulation has been further extended to a dual array-processing technique, Double BeamForming (DBF), that employs the diversity presented by having both source and receiver arrays to refine the acoustic signals into separate eigenray contributions, effectively transforming the information from the spatial-domain (array-elements) to the angular-domain (ray-paths).

A laboratory experiment was conducted in an ultrasonic waveguide in a tank environment, to directly observe the effect of surface displacements on acoustic transmissions. The data acquired with this setup was used to construct a map of acoustic sensitivity by perturbing points along the surface individually in a sequential manner.

The experimental result was then compared to a numerical model used to calculate the sensitivity for the given ultrasonic waveguide. The two independent pictures of surface-acoustic sensitivity show a great deal of agreement. Application of the DBF technique further refines the spatial picture of the surface sensitivity kernel, while also allowing the contributions of individual eigenrays, that maybe coincident in time on one element-pair, to be separated as well. With these SSKs in hand, and assuming independence among the individual surface point contributions, one could potentially invert for an aggregate surface structure from a given set of measured perturbations. To this goal, the use of acoustic arrays on both ends of the environment would provide the spatial diversity needed to increase spatial resolution along the surface, and the double-beamforming technique provides one such way to combine the data.

Acknowledgements

The text of this chapter is, in full, a reprint of material accepted for publication in *The Journal of the Acoustical Society of America*: Jit Sarkar, Christian Marandet, Philippe Roux, Shane Walker, Bruce D. Cornuelle, and William A. Kuperman, “Sensitivity kernel for surface scattering in a waveguide”. The dissertation author was the primary investigator and author of this paper.

References

- [1] William A Kuperman and F Ingenito. Attenuation of the coherent component of sound propagating in shallow water with rough boundaries. *J. Acoust. Soc. Am.*, 61(5):1178–1187, 1977.
- [2] F G Bass, V Freulicher, and I Fuks. Propagation in statistically irregular waveguides—Part I: Average field. *Antennas and Propagation, IEEE Transactions on*, 22(2):278 – 288, 1974.
- [3] William A Kuperman and Henrik Schmidt. Self-consistent perturbation approach to rough surface scattering in stratified elastic media. *J. Acoust. Soc. Am.*, 86(4):1511–1522, Oct 1989.
- [4] J A Ogilvy. Wave scattering from rough surfaces. *Reports on Progress in Physics*, 50(12):1553–1608, Jan 1987.
- [5] Eric I Thorsos. The validity of the Kirchhoff approximation for rough surface scattering using a Gaussian roughness spectrum. *J. Acoust. Soc. Am.*, 83(1):78–92, Jan 1988.
- [6] Eric I Thorsos and Darrell R Jackson. The validity of the perturbation approximation for rough surface scattering using a Gaussian roughness spectrum. *J. Acoust. Soc. Am.*, 86(1):261–277, Jan 1989.
- [7] Peter H Dahl. Forward scattering from the sea surface and the van Cittert–Zernike theorem. *J. Acoust. Soc. Am.*, 115(2):589–599, 2004.
- [8] C C Yang, G C Fennemore, and S T McDaniel. Scintillation index of the acoustic field forward scattered by a rough surface for two-and three-dimensional scattering geometries. *J. Acoust. Soc. Am.*, 91(4):1960–1966, 1992.
- [9] Victor Twersky. On the non-specular reflection of plane waves of sound. *J. Acoust. Soc. Am.*, 22(5):539–546, 1950.

- [10] Emmanuel K Skarsoulis and Bruce D Cornuelle. Travel-time sensitivity kernels in ocean acoustic tomography. *J. Acoust. Soc. Am.*, 116(1):227–238, 2004.
- [11] Jeroen Tromp, Carl Tape, and Qinya Liu. Seismic tomography, adjoint methods, time reversal and banana-doughnut kernels. *Geophys. J. Int.*, 160(1):195–216, Jan 2005.
- [12] Christian Marandet, Philippe Roux, Barbara Nicolas, and Jérôme I Mars. Target detection and localization in shallow water: An experimental demonstration of the acoustic barrier problem at the laboratory scale. *J. Acoust. Soc. Am.*, 129(1):85–97, 2011.
- [13] Ion Iturbe, Philippe Roux, Barbara Nicolas, Jean Virieux, and Jérôme I Mars. Shallow water tomography: Ray theory vs travel-time sensitivity kernels. *J. Acoust. Soc. Am.*, 125(4):2500–2500, 2009.
- [14] Matthew Dzieciuch, Peter Worcester, and Walter Munk. Turning point filters: Analysis of sound propagation on a gyre-scale. *J. Acoust. Soc. Am.*, 110(1):135–149, 2001.
- [15] Philippe Roux, William A Kuperman, William S Hodgkiss, Hee Chun Song, Tuncay Akal, and Mark Stevenson. A nonreciprocal implementation of time reversal in the ocean. *J. Acoust. Soc. Am.*, 116(2):1009–1015, 2004.

Chapter 5

Conclusions

The Born approximation to perturbations in the wave equation has been previously explored with respect to travel-time sensitivity of peak-arrivals in ocean acoustic propagation models. Chapter 2 extended this analysis to include the amplitude and phase of a demodulated broadband signal, and showed that amplitude does indeed contain more information about the ocean sound-speed structure over phase measurements alone - which were assumed to be directly relatable to travel-time changes. This was shown spectrally, via two-dimensional spatial transforms, which presented amplitude and phase having complimentary sensitivities; and also directly, through synthetic inversion examples, where the estimates obtained using both amplitude and phase measurements combined were an improvement over estimates made using either data type individually.

Chapter 3 continued this investigation into sensitivity analysis by including calculations of the travel-time sensitivity kernel (TSK). Variations in observed phase were assumed to be directly relatable to shifts in travel-time, yet their respective formulations for sensitivity are not apparently reconcilable, and even the visual appearance of each sensitivity map shows significant differences in spatial structure. The extra detail present in the TSK was investigated directly through perturbed numerical models, and shown to not actually be representative of travel-time variability; on the contrary, it resulted in changes to only the amplitude of the peak with no corresponding shifts in phase. A possible explanation for this discrepancy is suggested from the derivation of the TSK.

A numerical survey, conducted through a synthetic time-evolving ocean, explored the performance of these three sensitivity kernel types statistically, showing that phase was the most linear aspect of the observed acoustic response, and was estimated well by the phase sensitivity kernel. Additionally, the phase-derived measure of travel-time variations was shown to be a much better estimator than the TSK itself for large magnitude perturbations. In these same tests, the observed changes in amplitude often exhibited non-linearity at small magnitudes of sound-speed perturbations; but even in the apparently linear cases, the amplitude sensitivity kernel faired poorly as an estimator. However, the good agreement seen in a few of the examples shown suggests that amplitude information may still have potential, but might require more work to be useful — perhaps moving to higher-order terms in the Born approximation.

Chapter 4 applies these same perturbation methods to changes in the boundary conditions of a waveguide, in contrast to the volumetric sound-speed changes discussed in the earlier chapters. In this case, the Born approximation is used to estimate the acoustic response to point displacements along the air-water interface at the surface of the waveguide, and is shown to correspond well with the results of a laboratory tank experiment conducted at ultrasonic scale, in which the surface was displaced directly with a point-probe. While care must be taken with regard to any doppler effects introduced by a moving interface, this work still suggests the potential use of surface sensitivity analysis in inverting for a snapshot of the sea-surface shape.

Taken all together, sensitivity analysis of perturbations to the wave equation — both within the volume of the ocean, and to the interface at the surface — could theoretically be used to characterize ocean structure using a single combined linear inversion step, given only base numerical calculations through an appropriate mean picture of the environment. However, care must be taken to quantify the relative effects of surface vs volume disturbances, and to better understand if/when amplitude data can be incorporated. There may also be some applications for sensitivity kernels in work on underwater communications, with regards to channel equalization methods. Especially with respect to encoding methods us-

ing phase-shift keying (PSK), as the phase response to environmental variability is seen to be highly linear and could simplify deconvolution techniques. Finally, sensitivity analysis may be of most use simply as an efficient alternative to perturbed numerical forward models, for any purpose. During the course of this research, it was observed that such complex range-dependent simulations could take several hours, if not days to complete (e.g. for the time-evolving ocean), whereas the estimation process using the pre-calculated sensitivity kernels finished in just a few seconds/minutes.